Correspondence to:
M. S. Solano,
Miguel.Solano@usm.edu

Nonlinear Internal Tides in a Realistically Forced Global Ocean Simulation

Miguel S. Solano[1] [ID]**, Maarten C. Buijsman[1]** [ID]**, Jay F. Shriver[2]** [ID]**, Jorge Magalhaes[3]** [ID]**,
Jose da Silva[3]** [ID]**, Christopher Jackson[4], Brian K. Arbic[5]** [ID]**, and Roy Barkan[6,7]** [ID]

[1]School of Ocean Science and Engineering, The University of Southern Mississippi, Stennis Space Center, Bay St. Louis, MS, USA, [2]Naval Research Laboratory, Stennis Space Center, Bay St. Louis, MS, USA, [3]Faculty of Sciences University of Porto, Porto, Portugal, [4]Global Ocean Associates, Alexandria, VA, USA, [5]Department of Earth and Environmental Sciences, University of Michigan, Ann Arbor, MI, USA, [6]Porter School of the Environment and Earth Sciences, Tel Aviv University, Tel Aviv, Israel, [7]Department of Atmospheric and Ocean Sciences, University of California Los Angeles, Los Angeles, CA, USA

Abstract The decay of the low-mode internal tide due to the superharmonic energy cascade is investigated in a realistically forced global Hybrid Coordinate Ocean Model simulation with 1/25° (4 km) horizontal grid spacing. Time-mean and depth-integrated supertidal kinetic energy is found to be largest near low-latitude internal tide generation sites, such as the Bay of Bengal, Amazon Shelf, and Mascarene Ridge. The supertidal kinetic energy can make up to 50% of the total internal tide kinetic energy several hundred kilometers from the generation sites. As opposed to the tidal flux divergence, the supertidal flux divergence does not correlate with the barotropic to baroclinic energy conversion. Instead, the time-mean and depth-integrated supertidal flux divergence correlates with the nonlinear kinetic energy transfers from (sub)tidal to supertidal frequency bands as estimated with a novel coarse-graining approach. The regular spaced banding patterns of the surface-intensified nonlinear energy transfers are attributed to semidiurnal mode 1 and mode 2 internal waves that interfere constructively at the surface. This causes patches where both surface tidal kinetic energy and nonlinear energy transfers are elevated. The simulated internal tide off the Amazon Shelf steepens significantly near these patches, generating solitary-like waves in good agreement with Synthetic Aperture Radar imagery. Globally, we find that regions of high supertidal energy flux also show a high correlation with observed instances of internal solitary waves.

Plain Language Summary Ocean tides generate internal waves at steep ridges and continental shelves in a stratified ocean. In some regions with strong tidal forcing, surface intensified stratification, and weak background rotation, these waves are observed to steepen into solitary-like waves. In this process, energy is transferred from the tidal band to higher (supertidal) frequencies and wavenumbers. This study investigates "internal tide steepening" in a realistically forced global Hybrid Coordinate Ocean Model (HYCOM) simulation with a 4-km horizontal grid spacing. In our simulation, supertidal internal wave energy accounts for about 5% of the total energy available to internal tides equatorward of ±25°. However in some regions, such as the Amazon Shelf and Bay of Bengal, this ratio can be as much as 50%. Along the internal tide beams, the supertidal energy transfers are enhanced in regular spaced "patches" where longer and faster mode 1 semidiurnal internal tides overtake the shorter and slower mode 2 internal tides. In these patches the surface velocities of these waves constructively superpose, enhancing the surface kinetic energy and nonlinear energy transfers. At the Amazon Shelf, sharp-crested solitary-like waves that emerge in these patches in the HYCOM simulation are in good agreement with satellite observations. Although nonlinear internal tides are simulated in our global ocean model simulation, higher resolutions are needed to better resolve the energy cascade to smaller scales.

1. Introduction

Tidal internal waves (internal tides) are generated when barotropic flow interacts with topography at a rate of about 1 TW globally (Egbert & Ray, 2003). The internal tides play an important role in water-mass transformation due vertical mixing and advection (Assene et al., 2023; Jensen et al., 2020; Jithin & Francis, 2020; Waterhouse et al., 2014; You et al., 2021), affecting the thermohaline overturning circulation (Melet et al., 2013; Wunsch & Ferrari, 2004). While globally about half of the energy converted to internal tides is dissipated locally

Visualization: Miguel S. Solano
Writing – original draft: Miguel S. Solano, Maarten C. Buijsman
Writing – review & editing: Miguel S. Solano, Maarten C. Buijsman, Jay F. Shriver, Jorge Magalhaes, Jose da Silva, Christopher Jackson, Brian K. Arbic, Roy Barkan

as high vertical modes (Vic et al., 2019), the remaining low modes radiate away. In both satellite altimetry (Zhao et al., 2016) and realistically forced global ocean models (Buijsman et al., 2020; Muller et al., 2012; Shriver et al., 2012) low-mode internal tides are observed to propagate across ocean basins. The dissipation of these low-mode internal tides is attributed to several mechanisms: (a) scattering at topography (Johnston & Merrifield, 2003; Lamb, 2004; Mathur et al., 2014), (b) scattering by mesoscale eddies (Dunphy et al., 2017; Kelly et al., 2016; Savage et al., 2020), (c) breaking at topography and shelves (Klymak et al., 2016; Legg, 2014), and (d) wave-wave (or self) interactions (Baker & Sutherland, 2020; Eden et al., 2019; Olbers, 1976; Sutherland & Dhaliwal, 2022; Varma & Mathur, 2017).

In this paper we consider the decay of low-mode internal tides, generated at tall ridges or shelves, due to wave-wave interactions that drive a forward energy cascade to higher frequencies and wavenumbers. Linear internal tides manifest in the ocean as plane propagating wave modes that form horizontal wave beams. These modes can either self interact (Baker & Sutherland, 2020; Sutherland & Dhaliwal, 2022) or interact with other modes (Varma & Mathur, 2017) in resonant triad interactions, generating modes at higher frequencies and wavenumbers. A commonly studied triad interaction, in which an internal tide interacts with an inertial mode of half the tidal frequency, referred to as Parametric Subharmonic Instability (PSI; e.g., Ansong et al., 2018; Mackinnon et al., 2013), is not considered in this study.

When the background rotation is weak and the stratification is surface intensified, a low-mode internal tide with significant energy may undergo a "superharmonic cascade" (Sutherland & Dhaliwal, 2022), in which the mode disperses into a train of nonlinear internal waves (NLIW) (Gerkema & Zimmerman, 1995; Helfrich & Grimshaw, 2008), also referred to as solitons or solitary waves. These waves have higher wavenumbers and frequencies than the mother wave they evolved from. This process, in which a long sinusoidal internal tide transforms into a short wavelength solitary wave of $\mathcal{O}(1)$ km, is also referred to as "nonlinear steepening." Analytical solutions for these NLIW result from the modified Korteweg-de Vries (KdV) equations (Ostrovsky & Stepanyants, 1989), in which the advective term balances nonhydrostatic and Coriolis dispersion. Due to its higher frequency, the semidiurnal internal tide is more affected by nonlinear steepening than the diurnal internal tide (Farmer et al., 2009). Equatorward of the diurnal turning latitude, Coriolis dispersion inhibits the steepening of the diurnal internal tide because its frequency is closer to the local Coriolis frequency (Farmer et al., 2009; Helfrich & Grimshaw, 2008).

Nonlinear internal waves may also result from other mechanisms than the steepening of the low-mode internal tide. Among others, these mechanisms include tide-induced lee waves over topography (Farmer & Armi, 1999; Maxworthy, 1979), tidal beams impinging on a pycnocline (Gerkema, 2001; Grisouard et al., 2011; Mercier et al., 2012; New & Pingree, 1990, 1992), and topographic reflections and scattering (Gerkema et al., 2006; Lamb, 2004; Tabaei et al., 2005). However, we do not consider these mechanisms in this study.

Low-mode NLIW with large enough amplitudes in the interior are easily detectable with Synthetic Aperture Radar (SAR) and optical sunglint imagery from satellite (Alpers, 2018; Jackson et al., 2012, 2013) because the waves' surface current divergence and convergence affect ocean surface roughness. Using optical sunglint imagery, Jackson (2007) compiled a global map of NLIW that shows they are ubiquitous globally in coastal shelf areas and in the (sub)tropics in the open ocean, for example, in the South China Sea (Alford et al., 2015; Simmons et al., 2011), near the Mascarene Ridge (da Silva et al., 2015; Konyaev et al., 1995), in the Bay of Bengal and Andaman Sea (Jensen et al., 2020; Magalhaes et al., 2020; Osborne & Burch, 1980), and offshore of the Amazon Shelf (Ivanov et al., 1990; Magalhaes et al., 2016). The higher harmonic frequencies associated with these NLIW have also been observed with moorings, for example, in the Bay of Biscay (van Aken et al., 2007) and globally with surface drifters (Yu et al., 2019).

High-frequency nonlinear (solitary) internal waves have generally been studied in high-resolution process and regional nonhydrostatic model simulations with horizontal resolutions of $\mathcal{O}(100)$ m (e.g., Buijsman et al., 2010; da Silva et al., 2015; Magalhaes et al., 2020; Simmons et al., 2011). It is not yet clear how well they are simulated in realistically forced hydrostatic global ocean model simulations with horizontal resolutions of $\mathcal{O}(1)$ km. The appearance of solitary-like waves in hydrostatic models (Jensen et al., 2020) has been attributed to numerical dispersion that mimics the nonhydrostatic dispersion (Vitousek & Fringer, 2011). Global ocean models do simulate internal waves at supertidal frequencies (e.g., Arbic et al., 2022; Luecke et al., 2020; Müller et al., 2015; Savage et al., 2017). However, these studies have not specifically focused on tidally generated low-mode NLIW, which are the target of this paper. While the depth-integrated energy budget of the semidiurnal internal tide has

been well investigated in realistically forced global ocean simulations (Buijsman et al., 2016, 2020; Li & von Storch, 2020; Müller, 2013), such energy budget is lacking for low-mode NLIW that have evolved from the primary frequency internal tides.

The overarching goal of this paper is to understand the decay of low-mode internal tides due to nonlinear steepening that drives a forward energy cascade to supertidal frequencies in a global Hybrid Coordinate Ocean Model (HYCOM) simulation with a 4-km horizontal resolution (Raja et al., 2022). Specific goals of this study are to (a) quantify the kinetic energy in the supertidal band, (b) quantify the energy transfer rate from the tidal to supertidal frequencies, (c) identify the mechanisms responsible for these energy transfers, and (d) compare simulated hotspots of supertidal internal wave energy with observations of NLIW.

The paper layout is as follows: the ocean model and methods used for this study are briefly described in Section 2. Global internal tide energetics are presented in Section 3, and discussed in more detail for the main internal tide beam radiating from the Amazon Shelf. In Section 4 we correlate the occurrence of simulated supertidal energy flux with satellite imagery of solitary internal waves globally. We then estimate the nonlinear energy transfer rate from primary to higher-harmonic frequencies based on the coarse-grained kinetic energy transfer, and attribute the spatial patterns of the energy transfers to constructive interference between modes. Finally, we summarize our findings and make suggestions for future work in Section 5.

2. Model and Methods

2.1. Model

HYCOM is a primitive equation ocean general circulation model (Bleck, 2002) and the operational global ocean forecast model of the United States Navy (Metzger et al., 2014). The model uses a hybrid vertical coordinate that is isopycnal in the open ocean and transitions to terrain-following in shallow water, with z-coordinates used to resolve the surface mixed layer. The simulation presented in this paper is run in a forward (non-assimilative) mode on a tripolar grid at 1/25° (4 km) nominal horizontal resolution with 41 nonuniform layers in the vertical. In the mixed layer, vertical grid points are located at fixed depths most of which are 8 m apart, while in the deep ocean they move vertically with their assigned isopycnals. This grid resolution allows HYCOM to resolve at least four semidiurnal internal waves modes in deep water (Buijsman et al., 2020).

The model is forced with realistic atmospheric fields from the Navy Global Environmental Model (Hogan et al., 2014) and tidal forcing for the M_2, S_2, K_1, O_1, and N_2 tidal constituents. We select these five constituents because they account for the majority (>95%) of the tidal energy globally and they are easy to separate in frequency space for a time series with a duration of 30 days. To account for numerical errors in the tidal solution due to imperfect topography and damping terms, an Augmented State Ensemble Kalman Filter is applied to optimize the spatially varying Self Attraction and Loading term used in the simulations (Ngodock et al., 2016). The sea surface height root mean squared error with TPXO8-atlas, an altimetry constrained model, is 2.6 cm. The surface tidal error is minimized by tuning the strength of the linear wave drag (Jayne & St. Laurent, 2001), which is a parameterization of the surface-tide energy conversion to the unresolved baroclinic wave modes.

Model output from global HYCOM simulations has been validated extensively against moorings (Luecke et al., 2020), altimetry (Buijsman et al., 2016, 2020; Shriver et al., 2012), drifters (Arbic et al., 2022), and other models (Arbic et al., 2022; Savage et al., 2017). While these comparisons are favorable for the subtidal, inertial, and tidal bands, the 4-km simulations are still deficient in resolving motions at supertidal frequencies (Luecke et al., 2020; Savage et al., 2017; Siyanbola et al., 2023).

In this paper we demonstrate that our HYCOM simulation can resolve the initial stages of the superharmonic cascade associated with the decay of the low-mode internal tide. In Appendix A, we compare the generation of NLIW in the hydrostatic HYCOM simulation with a high-resolution nonhydrostatic MITgcm simulation at the Mascarene Ridge (da Silva et al., 2015) and show that our global HYCOM simulation does not resolve NLIW with wavelengths <8 km that can result from this cascade. We find that HYCOM underestimates the supertidal energy by about 50% at this location. Moreover, the hydrostatic approximation and horizontal and vertical grid spacings in our simulation do not allow for the full resolution of other nonlinear features such as (breaking) topograhic lee waves that occur near steeply sloping and shallow topography.
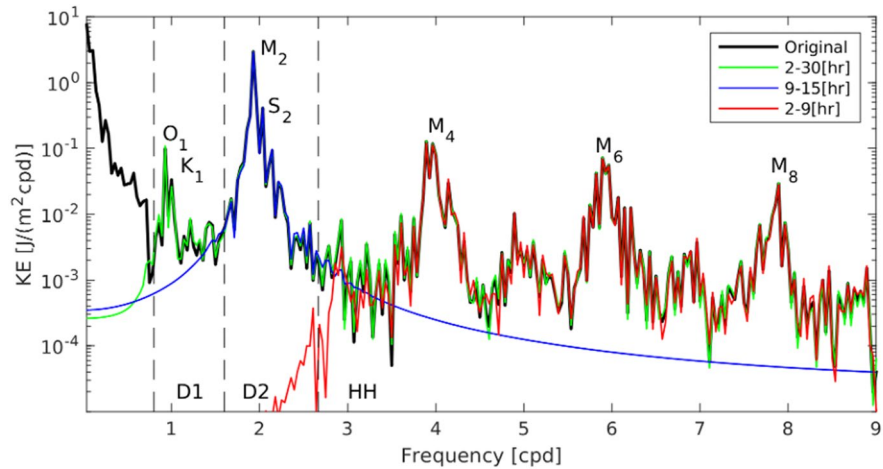
Figure 1. Kinetic energy spectra computed from Hybrid Coordinate Ocean Model baroclinic velocity at the surface (black) and band-passed filtered with 2–30 (green), 9–15 (blue), and 2–9 hr (red) cutoff periods. The spectrum is computed offshore the Amazon Shelf at 45°W and 3.5°N.

2.2. Filtering

We compute the energy terms for the filtered 3D fields from our global HYCOM simulation. We use hourly output from global HYCOM for a 30-day period, starting May 20 and ending 20 June 2019. We use a fourth order Butterworth band-pass filter with 2–30 (green), 9–15 (blue), and 2–9 hr (red) cutoff periods to evaluate total internal tide energy (D1 + D2 + HH), semidiurnal (D2), and higher-harmonic (HH) frequency bands, respectively. We remove the first and last days to avoid ringing effects such that fields are time-averaged over a 28-day period. Figure 1 shows the horizontal energy frequency spectra of baroclinic surface velocities offshore of the Amazon Shelf, where tidal peaks (D1, D2) and higher-harmonic (HH) peaks can be observed. The HH (supertidal) peaks occur at multiples of the primary tidal frequencies (e.g., at 3, 4, 5, 6, etc., cycles per day; cpd).

Because internal tide energy is found at narrow-band peaks, energy estimates are not very sensitive to the choice of the cutoff frequencies. The 30-day simulation period with hourly output frequency restricts our analysis to motions with a minimum fundamental frequency of 1/30 cpd and a maximum Nyquist frequency of 12 cpd, which captures our lowest frequency of interest (D1) and at least the first few supertidal peaks (D3–D6). The simulation period also allows for two spring-neap cycles, which is important for the generation cycle of nonlinear internal tides.

The supertidal band of energy spectra in most of the global ocean is dominated by the M_4, M_6, etc., higher harmonics (e.g., Figure 1), because M_2 is the dominant constituent (Egbert & Ray, 2003). Hence, in the discussion section we focus on the nonlinear energy transfers out of semidiurnal band. However, in areas where both diurnal and semidiurnal surface tides are important, for example, in the western Pacific and South China Sea (Wang et al., 2021; Zhao, 2014), terdiurnal (3 cpd) internal tides can also be generated (Chen et al., 2021). We also observe these terdiurnal peaks in our spectra (not shown), but they are generally lower than the M_4 peaks. Terdiurnal internal tides may result from the nonlinear interaction between the semidiurnal and diurnal internal tides. However, this type of interaction is not discussed in this paper.

2.3. Internal Wave Energetics

We apply the depth-integrated internal wave energy balance as derived by Kang and Fringer (2012) to baroclinic waves in both the tidal and supertidal bands. It is written as

$$\overline{C} = \frac{\partial \overline{E}}{\partial t} + \nabla_H \cdot \overline{\mathbf{F}} + \overline{R}, \tag{1}$$

where the overbars indicate depth-integration, $\overline{C}$ is the barotropic to baroclinic energy conversion, $\frac{\partial \overline{E}}{\partial t}$ is the tendency term, $\nabla_H = \left(\frac{\partial}{\partial x}, \frac{\partial}{\partial y}\right)$ is the horizontal divergence operator, $\overline{\mathbf{F}}$ is the depth integrated baroclinic energy

flux vector, and $\overline{R}$ is the residual. In the absence of wave-mean flow and wave-wave energy exchange terms (Barkan et al., 2021; Kelly, 2016; Pan et al., 2021), the residual term is interpreted as baroclinic energy dissipation (Buijsman et al., 2016).

The total baroclinic wave energy $\left(\overline{E}\right)$ in Equation 1 is the sum of the horizontal wave kinetic energy $\left(\overline{KE}\right)$ and available potential energy $\left(\overline{APE}\right)$. For a water column height (h), the horizontal wave kinetic energy is computed as

$$\overline{KE} = \frac{1}{2}\rho_0 \int_{-h}^{0} |\mathbf{u}'_H|^2 \, dz, \tag{2}$$

where ρ_0 is the reference density and $\mathbf{u}'_H = (u', v')$ the baroclinic horizontal velocity vector along the x and y coordinates. The linear form of available potential energy is computed as (Kang & Fringer, 2010)

$$\overline{APE} = \frac{1}{2}\rho_0 \int_{-h}^{0} N(z)^2 \xi(z)^2 \, dz, \tag{3}$$

where ξ is the vertical isopycnal displacement and $N(z)$ is the background buoyancy frequency. Although maps of time-mean $\overline{APE}$ feature similar patterns as time-mean $\overline{KE}$, we only present maps of time-mean $\overline{KE}$ because maps of time-mean $\overline{APE}$ are noisy.

The depth-integrated hydrostatic baroclinic energy flux $\overline{F}$ is a measure of the horizontal internal wave energy transport. It can be written as

$$\mathbf{\overline{F}} = \overline{\mathbf{u}'_H E} + \overline{\mathbf{u}'_H p'}, \tag{4}$$

where $\mathbf{F_a} = \overline{\mathbf{u}'_H E}$ represents nonlinear self-advection, $\mathbf{F_p} = \overline{\mathbf{u}'_H p'}$ represents hydrostatic pressure work, and p' the perturbation pressure. The perturbation velocities and pressure have depth-integrals that are equal to zero, and are computed as described in Nash et al. (2005). Although advective energy fluxes can be as large as pressure fluxes in strongly nonlinear waves in high resolution Large Eddy Simulations (Venayagamoorthy & Fringer, 2005), we will show that the contribution from energy advection is small in our HYCOM simulation.

The barotropic to baroclinic conversion is a source term in Equation 1 and in the absence of nonhydrostatic effects can be computed as

$$\overline{C} = -p(z = -h)\overline{\mathbf{u}_H} \cdot \nabla_H h, \tag{5}$$

where $\nabla_H h$ is the horizontal gradient of the ocean seafloor depth.

Finally, after time averaging Equation 1 over multiple tidal cycles, the internal wave energy budget is

$$\langle \overline{C} \rangle = \nabla_H \cdot \langle \mathbf{\overline{F}} \rangle + \langle \overline{R} \rangle. \tag{6}$$

We apply this budget separately to both the tidal and supertidal bands.

3. Results

In this section we discuss the geographical distribution of internal tide energy in the deep ocean, neglecting areas shallower than 250 m, and then explore energy sources and sinks. We limit our analysis to low-latitudes, between 25°S and 25°N, to provide more detail where higher-harmonic energy is important and to avoid aliasing of high frequency motions due to mesoscale eddies and near-inertial waves.

3.1. Global Energetics

The time mean of the depth-integrated baroclinic kinetic energy (Equation 2) is shown in Figure 2 for the (a) diurnal, (b) semidiurnal, and (c) higher-harmonic (supertidal) frequency bands. To highlight regions where supertidal waves are important, the ratio of higher-harmonic to total tidal energy (D1 + D2 + HH) is plotted in Figure 2d. The *KE* in the diurnal band has contributions from both diurnal internal tides and equatorward propagating
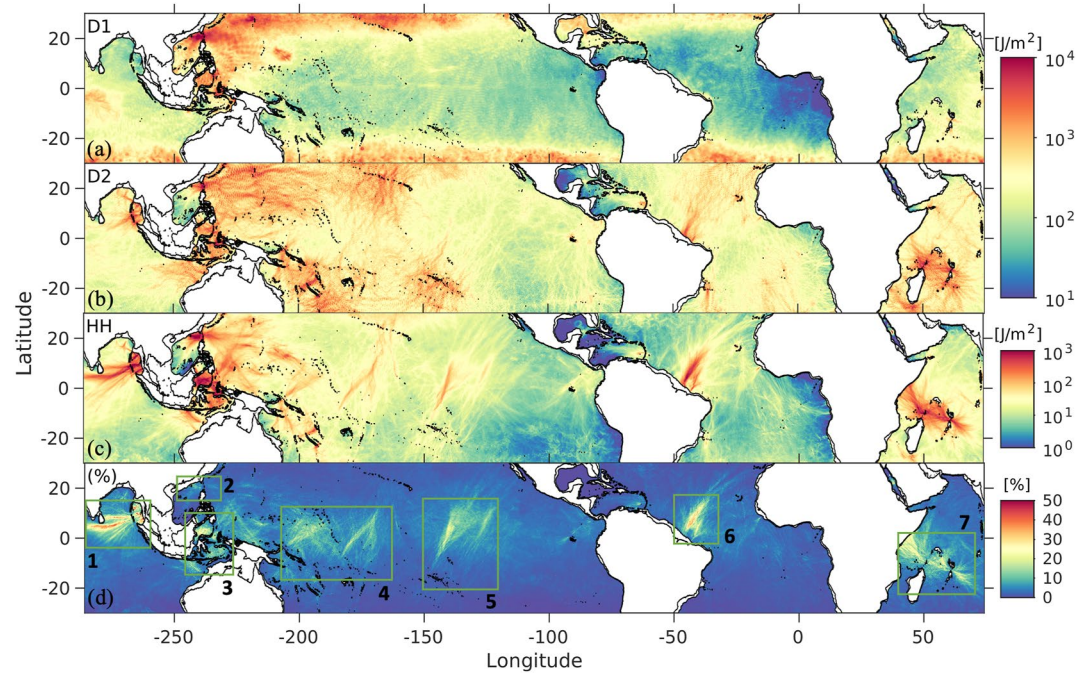
Figure 2. Time-mean and depth-integrated internal wave kinetic energy (J/m^2) in the (a) diurnal (D1), (b) semidiurnal (D2), and (c) supertidal (HH) frequency bands. (d) The ratio of supertidal (KE_{HH}) to total (KE_{tot}) energy as a percentage. Regions of interest are indicated by the green rectangles: (1) Bay of Bengal, (2) Luzon Strait, (3) Indonesian Archipelago, (4) West Pacific Islands, (5) French Polynesian Islands, (6) Amazon Shelf, and (7) Seychelles and Mascarene Ridge. The black contours mark seafloor depths at 0 and 250 m.

near-inertial waves generated near the critical latitudes (±30°). Diurnal internal tides are most prominent at the Luzon Strait and Indonesian Archipelago (rectangles 2 and 3 in Figure 2d), while semidiurnal energy is more ubiquitous in the global ocean. In the HYCOM simulation analyzed here, supertidal KE is 1–2 orders of magnitude lower than tidal energy almost everywhere, except along strong internal tide beams at low-latitudes, most notably at the Bay of Bengal and Amazon Shelf (rectangles 1 and 6 in Figure 2d), where supertidal energy makes up 30%–50% of the total energy.

The spatial distribution of tidal and supertidal KE yields insight into the generation of the internal waves. KE at diurnal and semidiurnal frequencies is highest near shallow and steep ridges, where energy is transferred from barotropic to baroclinic modes, and then decays rapidly with distance from the source. Conversely, supertidal KE can peak away from the internal tide generation sites, suggesting that the source of supertidal KE is the propagating internal tide. For example, equatorward of Hawaii (rectangle 4 in Figure 2d) and equatorward of the French Polynesian Islands (FPI; rectangle 5 in Figure 2d), supertidal KE emerges several hundred kilometers away from the generation sites of the primary internal tide. The supertidal KE fraction is much smaller for beams radiating poleward from Hawaii and the FPI (Figure 2d). The asymmetry between equatorward and poleward radiating supertidal beams from Hawaii and FPI suggests that the Coriolis and buoyancy frequencies play an important role in the generation of superharmonics (Gerkema & Zimmerman, 1995; Sutherland & Dhaliwal, 2022).

The magnitudes of the depth-integrated and time-averaged horizontal tidal and HH pressure and advective fluxes are presented in Figure 3. The energy flux is dominated by pressure work and resembles the distribution of KE in both frequency bands (Figures 3a and 3b). Higher-harmonic fluxes in Figure 3b feature beams of $\mathcal{O}(1)$ kW/m appearing some distance away from the generation sites and remaining steady for several hundred kilometers. The tidal band advective flux in Figure 3c is $\mathcal{O}(10)$ W/m, which is negligible compared to the tidal pressure flux. In contrast, the advective flux in the supertidal band in Figure 3d is larger than in the tidal band and correlates well with the supertidal pressure flux and kinetic energy beams in the equatorial region. In these regions, internal tides have transferred a significant portion of their energy to waves at higher wavenumbers and frequencies, which contribute more to the nonlinear advective fluxes.
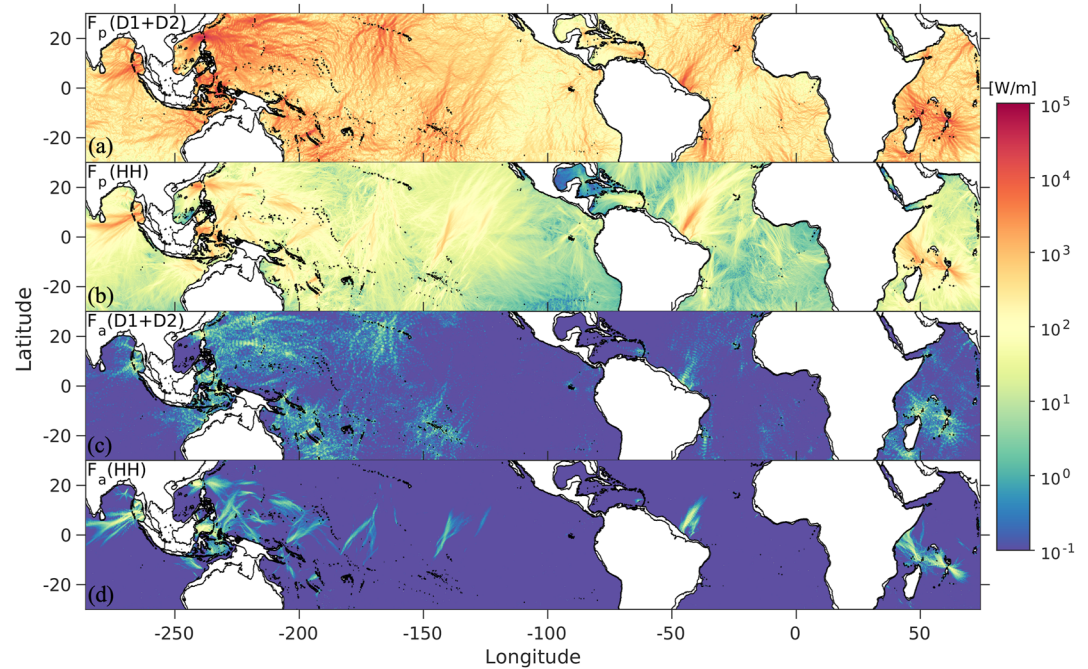
Figure 3. Time-mean and depth-integrated horizontal energy flux magnitude (W/m) of the (a) tidal (9–30 hr band-pass) pressure flux, (b) supertidal (9 hr high-pass) pressure flux, (c) tidal advective flux, and (d) supertidal advective flux. The black contours mark seafloor depths at 0 and 250 m.

To better understand the latitudinal dependence, we zonally integrate various energy terms using 1° bins from 25°S to 25°N (Figure 4). On average, supertidal KE accounts for 5% of the total internal tide KE at low-latitudes. It gradually increases from the mid to low latitudes reaching the largest value of about 10% at 4°N (Figure 4a), likely due to contributions from the Bay of Bengal and the Amazon Shelf (Figure 2d). The peak in diurnal KE near 20°N is attributed to the internal tide generation in Luzon Strait (rectangle 2 in Figure 2d). Diurnal KE increases poleward toward the diurnal turning latitudes due to adulteration by near-inertial waves. Globally integrating between $\pm25°$, we estimate that $KE_{tot} = 113.2$ PJ, where $KE_{D1} = 31.7$ PJ, $KE_{D2} = 76.1$ PJ and $KE_{HH} = 5.4$ PJ. Figure 4b shows that most of the energy converted from the surface to the baroclinic tide is input at semidiurnal frequencies (440 GW) as opposed to diurnal frequencies (60 GW), with a negligible amount converted to supertidal frequencies. The residuals of the tidal and supertidal energy budgets (Equation 6) in Figure 4c are positive for the tidal band, mostly due to dissipation, and negative for the supertidal band, suggesting a source term is missing. To better understand how internal tide energy at the primary frequencies is transferred to supertidal frequencies, we analyze the energetics along the main internal tide beam generated at the Amazon Shelf in the next section.

3.2. Energetics at the Amazon Shelf

The Amazon Shelf region (rectangle 6 in Figure 2d) features an energetic internal tide beam, in which up to half of the internal tide energy is in the supertidal band. In this beam, nonlinear internal solitary waves appear about 500 km from the coastline, coinciding with the rapid decay of the primary tide energy fluxes (Magalhaes et al., 2016). The direction of the main wave beam is modulated by the boundary currents along the shelf, namely the North Brazil Current and North Equatorial Counter Current (Magalhaes et al., 2016; Tchilibou et al., 2022). In this section we analyze the energy budget terms along the main internal tide beam generated at the Amazon Shelf to indicate potential sources of supertidal energy.

The main internal tide beam is generated in at least three hot spots along the steep Amazon Shelf slope (Figure 5a), in agreement with previous studies (Magalhaes et al., 2016; Tchilibou et al., 2022). The tidal energy flux is high at the shelf slope and along the internal tide propagation path with values >14 kW/m. The supertidal energy flux in Figure 5b is much lower at the shelf slope but increases significantly between 200 and 500 km from the
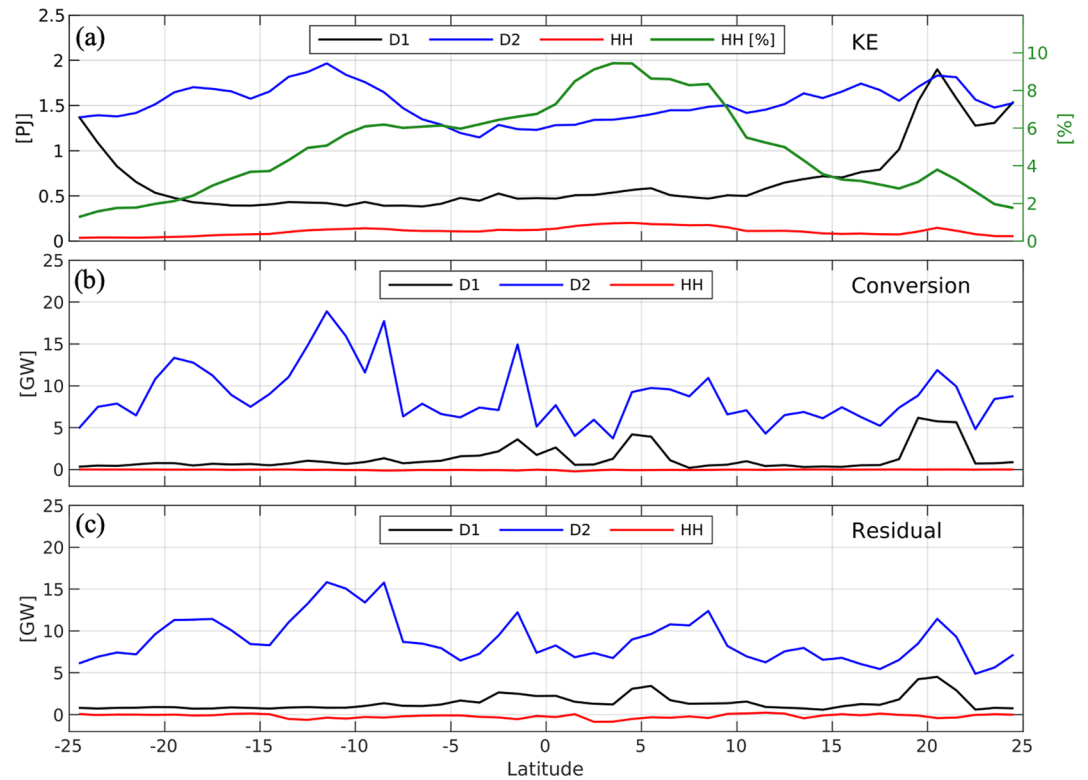
Figure 4. Zonally integrated band-passed energetics for 1° bins, from 25°S to 25°N. (a) Kinetic energy (left axis) and the percentage of supertidal *KE* (right axis). (b) Barotropic to baroclinic energy conversion. (c) The residual, computed as the difference between conversion and flux divergence (Equation 6).
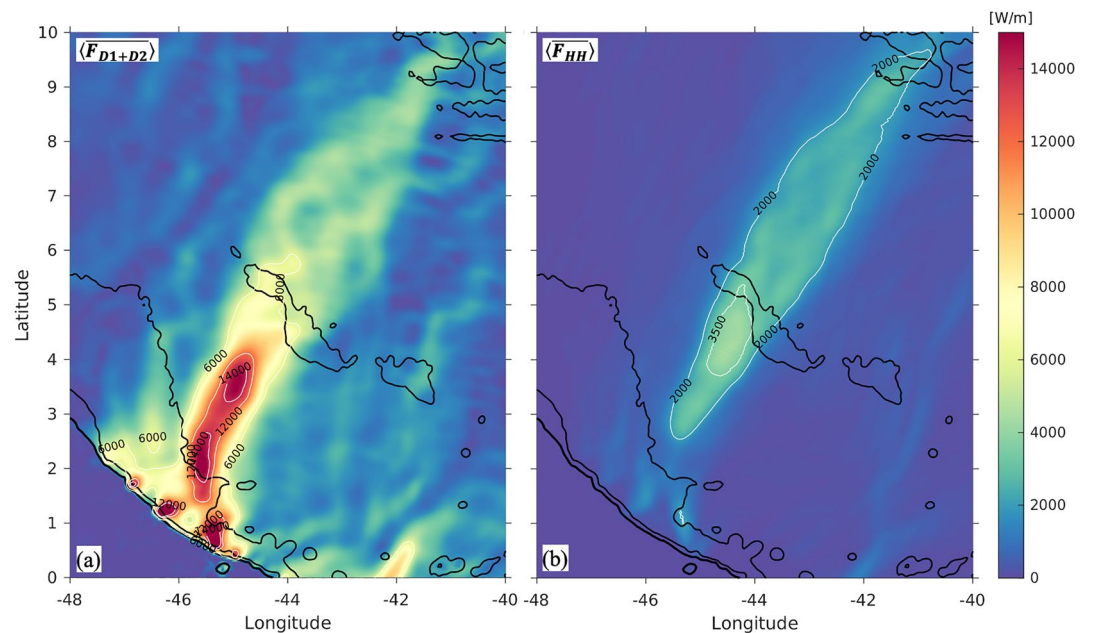

Figure 5. Time-averaged and depth-integrated horizontal energy fluxes band-passed over (a) tidal and (b) supertidal frequencies at the Amazon Shelf. Thin white contour lines are plotted at 6, 12, and 14 kW/m for the tidal energy fluxes, and 2 and 3.5 kW/m for the supertidal energy fluxes. Black contour lines mark the 250, 1,000, and 3,500 m seafloor depths.
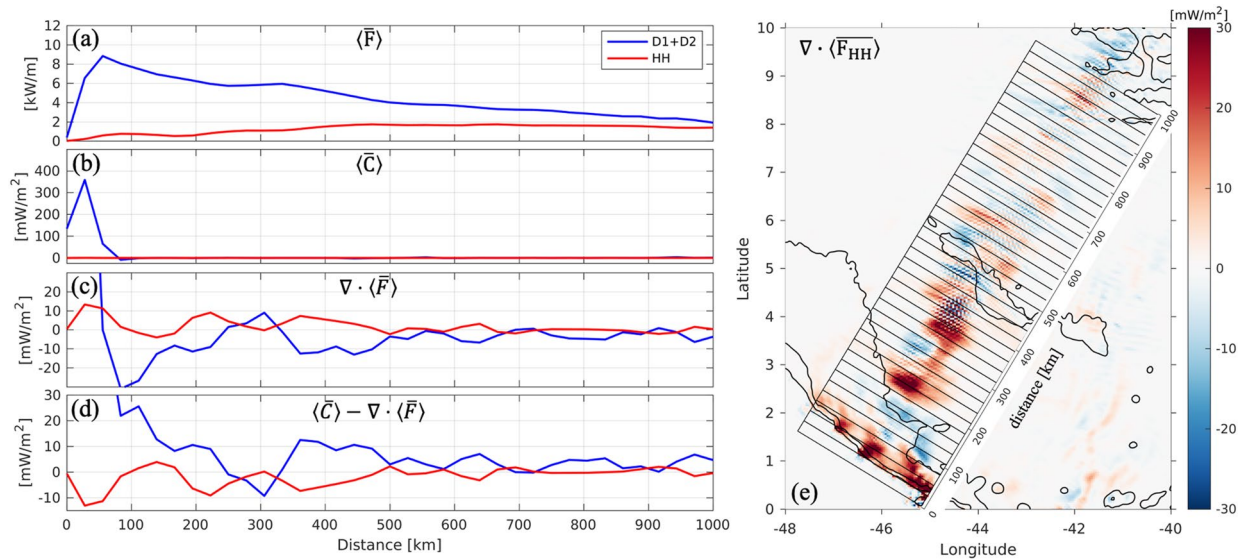
Figure 6. Depth-integrated, time-mean, and bin-averaged tidal and supertidal energy budget terms along the main internal tide beam at the Amazon Shelf: (a) energy flux, (b) conversion, (c) flux divergence, and (d) residual. (e) The time-mean and depth-integrated supertidal energy flux divergence. The black rectangles indicate the bins over which the energy terms are averaged. The black curves are the 250, 1,000, and 3,500 m seafloor-depth contours.

shelf break and then remains relatively steady at ~2 kW/m until the Mid-Atlantic Ridge (top right contours in Figure 5b).

To understand the spatial distribution of energy sources and sinks, we analyze the baroclinic energy budget (Equation 6) for the tidal and supertidal bands averaged over rectangular bins of 0.5° by 1.5° (55.5 by 166.5 km) along the main internal tide beam. The bins are shown in Figure 6e superimposed over supertidal flux divergence, where sources (sinks) are represented by the red (blue) colors. The bin-averaged energy flux in Figure 6a is largest for the tidal band. It has a maximum value of ~9 kW/m at the shelf slope and is attributed to the large tidal barotropic to baroclinic energy conversion in Figure 6b. On the contrary, the supertidal energy flux is initially low and increases offshore until it peaks at ~2 kW/m about 500 km from the slope. This increase does not coincide with the supertidal barotropic to baroclinic conversion, which is negligible in Figure 6b.

The decay of the tidal energy flux and the growth of the supertidal flux is more easily distinguished with the bin-averaged horizontal flux divergence in Figure 6c. Along the propagation path, the energy flux divergence at the primary and higher-harmonic frequencies appears to be anti-correlated, suggesting that energy is transferred from tidal to supertidal frequencies (and vice versa) at intervals spaced roughly 150 km apart, for example, near 220 and 370 km (near 130 and 300 km).

The residual $\langle \overline{R} \rangle$ of the energy balance (Equation 6) for the tidal band is generally positive in Figure 6d, in agreement with the overall decay of the flux in Figure 6a. The tidal residual is negative near 300 km, suggesting that terms may be missing, for example, due to wave-mean flow advection (Kelly et al., 2016) or energy exchanges between different frequency bands (Barkan et al., 2021; Kelly et al., 2016). Although wave-mean flow interactions are not the focus of this study, they may be a source or sink of energy for internal tides in the presence of mesoscale currents, such as the North Equatorial Counter Current and North Brazil Current. As in Figure 4, the supertidal residual is mostly negative, implying that an important source term is not accounted for. The mostly negative supertidal residual term and the spatial correlation between the tidal and supertidal flux divergence and residual terms suggest a net energy flux from the tidal to the supertidal band. This energy exchange will be investigated in more detail in the discussion section.

3.3. Solitary Waves at the Amazon Shelf

In HYCOM, the internal tide at the Amazon Shelf steepens into solitary-like waves near 400 km (Figure 7a), coinciding with the second patch of positive supertidal flux divergence (Figure 6e). At this location, the SSSH in Figure 7a and the thermocline displacement in Figure 7c feature the largest amplitudes and steepest slopes.
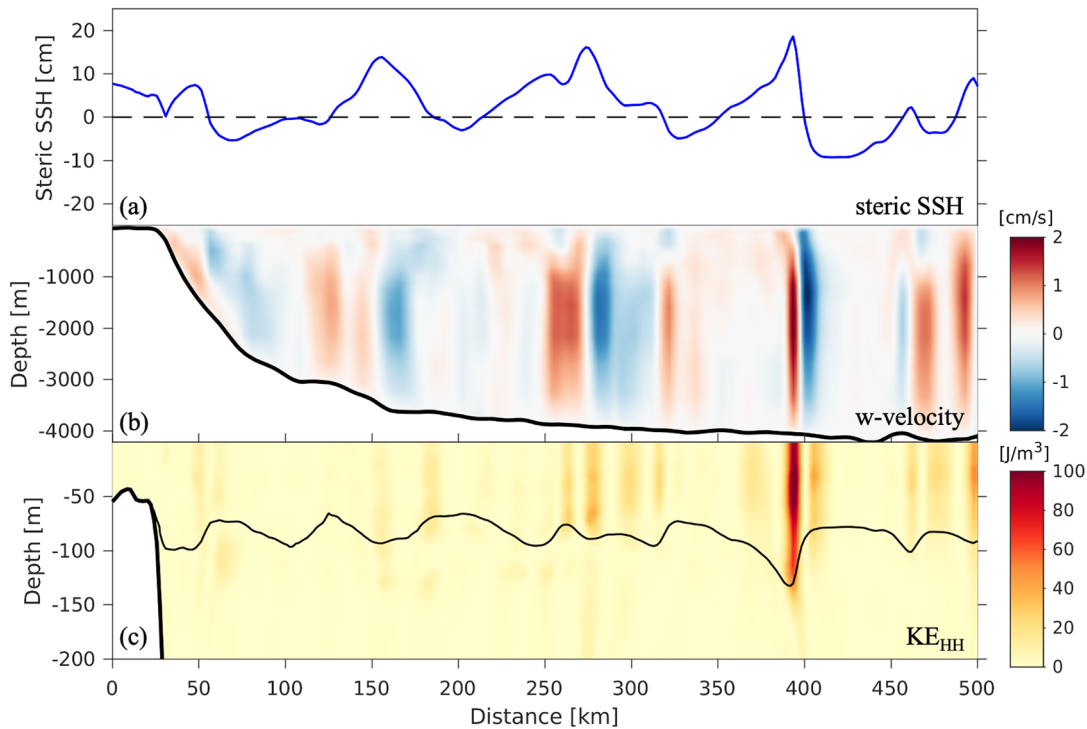
Figure 7. Snapshot of (a) 30-hr high-pass filtered steric sea surface height, (b) 30-hr high-pass filtered vertical velocity, and (c) higher-harmonic (9-hr high-passed) kinetic energy during an instance of internal tide steepening and solitary-like wave generation. The thick black line in panels (b, c) indicates the bottom bathymetry and the thin line in panel (c) indicates the pycnocline. The vertical scale used in panel (b) is different than in panel (c) to highlight the vertical velocity at depth and the kinetic energy near the surface, respectively.

Simultaneously, the vertical velocities at depth in Figure 7b and the supertidal kinetic energy at the surface in Figure 7b are enhanced. The distance between the SSSH peaks is about 110 km, which is the mode 1 wavelength at this location.

To validate the accuracy of the simulated solitary-like waves near the Amazon Shelf, we compare SSSH fields from HYCOM with crests extracted from SAR imagery (magenta lines) in Figure 8 during the same time-period (May-June). The internal wave crests in HYCOM steepen in regions where the solitary NLIW are observed. The satellite derived solitary waves emerge around 4°N and 44.5°W, roughly 400 km from the shelf break (see also Figure 7). These figures show that in HYCOM, large amplitude internal tides steepen into solitary-like waves as they propagate offshore in regions where supertidal energy is relatively large, in good agreement with satellite observations.

4. Discussion

In this section we further discuss the correlation between supertidal energy in the global HYCOM simulation and the observations of solitary waves in the global ocean, we estimate the nonlinear energy transfers to supertidal frequencies using a coarse-graining approach, and we attribute the spatio-temporal modulation of the nonlinear energy transfers to constructive interference between modes.

4.1. Comparison With Global Observations of NLIW

For the Amazon region we have shown that a strong supertidal energy flux of $\mathcal{O}(1)$ kW/m coincides with NLIW that are both simulated in HYCOM and observed in SAR images. To confirm this correlation globally, we compare the supertidal energy flux with the locations of NLIW observed by the 250 m Moderate-Resolution Imaging Spectrometer (MODIS) satellite over a 4-year period (Jackson, 2007) in Figure 9. Most regions in the deep ocean with supertidal energy fluxes >1 kW/m (purple shading in Figure 9), such as the Bay of Bengal, Andaman Sea, South China Sea, Indonesian Archipelago, Amazon Shelf, and Mascarene Ridge, agree well with
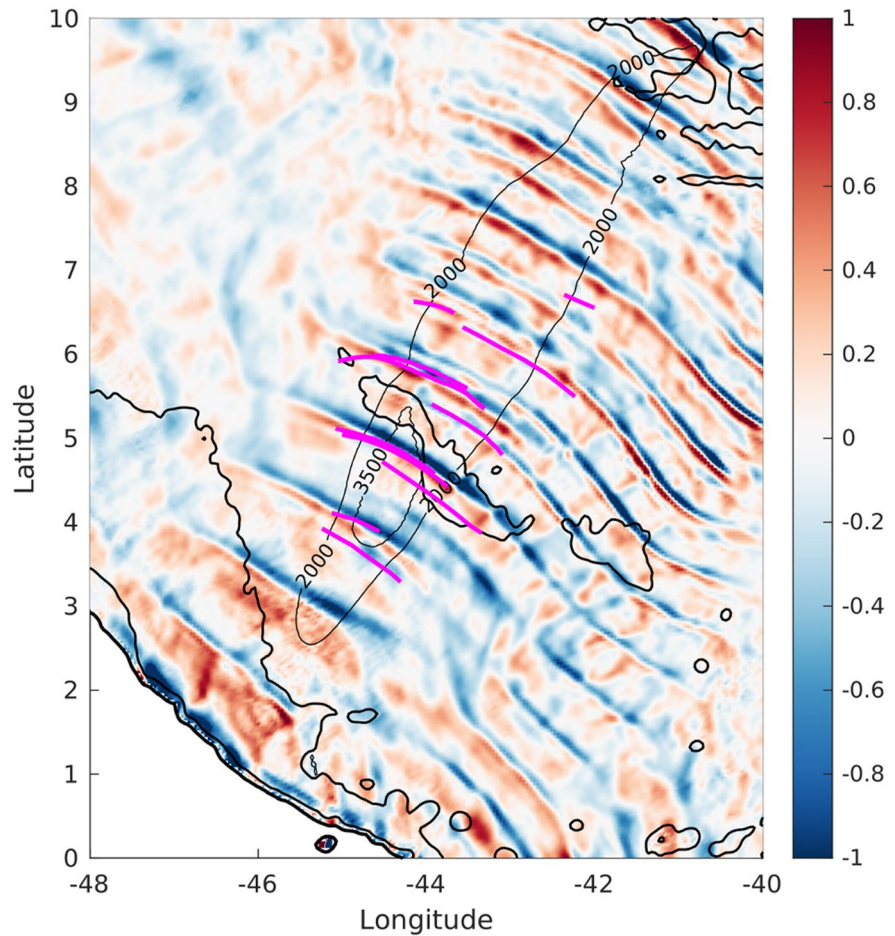
Figure 8. Snapshot of the normalized steric sea-surface height gradient along the northeast direction from Hybrid Coordinate Ocean Model and superposed crests of solitary waves derived from Synthetic Aperture Radar imagery as magenta lines. The thin black contours show the time-mean and depth-integrated supertidal energy flux at 2 and 3.5 kW/m. The thicker black contours mark the seafloor depths at 250, 1,000, and 3,500 m.

the locations of the observed solitary waves. However, solitary waves are also detected in regions with relatively low supertidal energy flux, such as over large areas in the eastern Atlantic and Pacific Oceans (rectangles 8 and 9 in Figure 9b) and on the continental shelves. In a recent study, Santos-Ferreira et al. (2023) showed that the solitary waves in the eastern Pacific evolve from gravity currents associated with tropical instability waves. The discrepancy between HYCOM and MODIS in rectangles 8 and 9 in Figure 9b may also be explained by weaker surface tides and/or unresolved bathymetric features in the HYCOM simulation, which may cause weaker primary and higher-harmonic internal wave flux beams. NLIW on shelves generally feature smaller wavelengths and energy fluxes (<1 kW/m) than in the open ocean. Hence, these waves are not well resolved in our HYCOM simulations, as opposed to the satellite images, which horizontal resolution is about eight times finer.

4.2. Nonlinear Energy Cross-Scale Transfers

The negative residuals of supertidal energy at the Amazon Shelf in Figures 4c, 6d, and 6e, point to a missing source term in the higher-harmonic energy budget. Therefore, we diagnose the nonlinear energy wave transfers as a function of time and space in HYCOM with a coarse-graining approach (Eyink & Aluie, 2009). The coarse-graining method has been used in physical oceanography to map the energy cascade in the North Atlantic (Aluie et al., 2018) and to quantify the energy transfer between mesoscale eddies and internal waves (Barkan et al., 2021). To our knowledge, the coarse-graining method has not yet been used to study the energy pathways of internal tides in the global ocean. Our use of the coarse-graining method here is therefore novel.
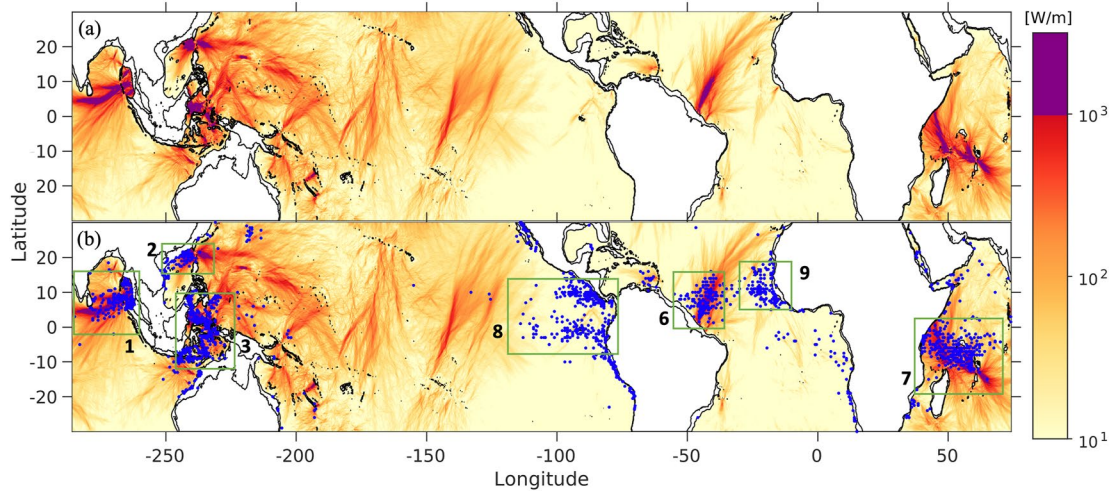
Figure 9. (a, b) Colormaps of time-mean and depth-integrated supertidal energy fluxes in global Hybrid Coordinate Ocean Model on a logarithmic scale compared with (b) observations of nonlinear internal waves (blue dots) captured by 250-m resolution Moderate-Resolution Imaging Spectrometer imagery. The green rectangles indicate regions of significant nonlinear internal wave activity due to tides: (1) Bay of Bengal and Andaman Sea, (2) Luzon Strait, (3) the Indonesian Archipelago, (6) Amazon Shelf, and (7) Seychelles and Mascarene Ridge, and due to non-tidal sources: (8) the eastern Pacific and (9) the eastern Atlantic.

Coarse-graining can be used to quantify energy transfers across an arbitrary length or time scale τ. The coarse-grained kinetic energy transfer (W/m^3) can be written in index notation as:

$$\Pi_\tau(x,t) = -\rho_0 \left(\widetilde{u_i u_j} - \tilde{u}_i \tilde{u}_j \right) \frac{\partial \tilde{u}_i}{\partial x_j} \tag{7}$$

where $i = 1, 2, 3$ and $j = 1, 2$ are indices indicating directions (x, y, z) and $\widetilde{(\cdot)}$ denotes the low-pass filter of quantity $(\cdot)$ with cutoff period τ. We use $\tau = 9$ hr (2.67 cpd) as our cutoff period (frequency), such that Π_τ represents the energy transfer rate between (sub)tidal and supertidal frequencies. However, we conclude from our results that the majority of this energy transfer likely comes from the semidiurnal internal tide.

In the absence of topographic conversion we now can approximate the HH energy balance as

$$\langle \overline{\Pi_\tau} \rangle = \nabla_h \cdot \langle \overline{\mathbf{F}_{HH}} \rangle + \langle \overline{R} \rangle \tag{8}$$

where the residual $\langle \overline{R} \rangle$ includes terms such as the dissipation and wave-mean flow interaction terms.

We compare the nonlinear cross-scale energy transfer to the divergence of the supertidal flux in three areas with strong HH energy fluxes in Figures 10a–10f: the Bay of Bengal, the Amazon Shelf, and Mascarene Ridge. In Appendix B, we compute commonly used nonlinear internal wave parameters for these sites to provide some context. In agreement with Figure 2d, these nonlinear parameters are largest for the Bay of Bengal. To reduce noise due to aliasing of high frequency motions, we average the supertidal flux divergence over a nine grid point stencil in Figure 10d, which yields a smoother appearance than the flux divergence in Figure 6e. The positive regions of cross-scale energy transfer indicate a forward cascade from tidal to supertidal frequencies, and they coincide with estimates of supertidal energy flux divergence. The energy transfer in all 3 regions in Figures 10a–10c is mostly forward and form a banding pattern along the propagation path of the internal tides at regularly spaced intervals separated by a distance longer than the mode 1 wavelength.

One goal of this paper is to estimate the nonlinear *KE* transfers from tidal to supertidal frequencies. After time-averaging and area integrating between $\pm 25°$, we compute 44.5 GW forward and 7.5 GW inverse transfers from (sub)tidal to higher-harmonic frequencies. This implies that about 7% of the energy converted from barotropic to baroclinic tides ($\sim$500 GW) between $\pm 25°$ cascades to higher-harmonics in the deep ocean, assuming that most of these energy transfers come from the primary tides.
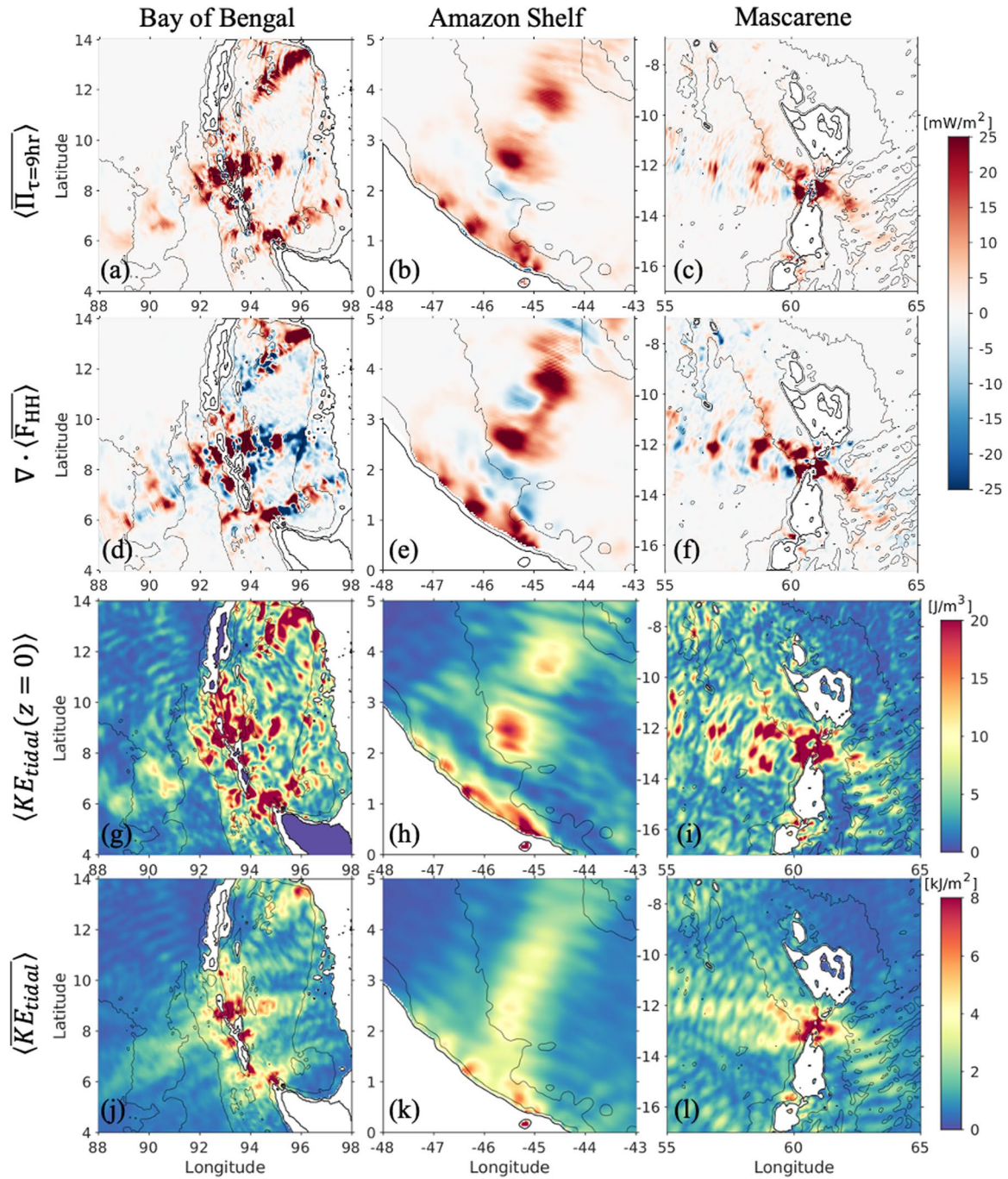
Figure 10. Time-mean and depth-integrated nonlinear energy transfer at (a) the Bay of Bengal and Andaman Sea, (b) the Amazon Shelf, and (c) the Mascarene Ridge. The time-mean and (d–f) depth-integrated supertidal energy flux divergence, (g–i) surface tidal (D1 + D2) kinetic energy, and (j–l) depth-integrated tidal (D1 + D2) kinetic energy for the same three areas. The contour lines mark the 0, 250, 1,000, and 3,500 m sea-floor depths.

4.3. Spatial Modulation of Nonlinear Energy Transfers

In this section, we investigate the mechanisms that cause the regularly spaced banding patterns in the supertidal flux divergence and the nonlinear cross-scale energy transfers. A similar banding pattern is also visible in tidally band-passed surface kinetic energy (Figures 10g–10i), while it is not present in the depth-integrated tidal KE (Figures 10j–10l). Although we compute KE for the tidal (D1 + D2) band in Figures 10g–10l, the banding patterns of time-mean KE are mostly due to the semidiurnal tides (not shown), which are the most dominant at

these internal tide hotspots (Figures 2a and 2b). In this banding pattern, the patches of large tidal surface *KE* also coincide with large nonlinear energy transfers. This is analogous to internal-wave dissipation scaling with energy density (e.g., Pollmann et al., 2017) because shear-driven turbulent internal wave dissipation is the end result of a forward energy cascade due to wave-wave interactions. The spatial patchiness of $KE(x, y, z)$ is attributed to the horizontal and vertical shear in the tidal baroclinic velocities, which drive the nonlinear energy transfers in Equation 7. The difference in banding patterns between surface *KE* and depth-integrated *KE* suggests that the banding patterns are caused by constructive and destructive interference between semidiurnal mode 1 and mode 2 waves, which are generally the most energetic waves generated at tall ridges and shelves in 4-km HYCOM simulations (see Figures 8f and 8g of Buijsman et al., 2020).

We decompose the baroclinic fields into vertical modes to demonstrate that the banding pattern in Figure 10 can be attributed to the interference patterns between semidiurnal mode 1 and mode 2 waves. We adopt the modal amplitude time series for baroclinic velocity $\hat{\mathbf{u}}_n(x, y, t)$ and pressure $\hat{p}_n(x, y, t)$, the normalized horizontal velocity eigenfunctions $\mathcal{U}_n(x, y, z)$, and eigenspeeds c_n as computed by Raja et al. (2022) for the same HYCOM simulation used in this study.

The kinetic energy density for any frequency band at a given depth and time for the sum of the mode 1 and 2 velocities reads (omitting *z* and *t* on the right-hand side (rhs) and *x* and *y* everywhere)

$$
\begin{aligned}
KE(z, t) &= \frac{1}{2}\rho_0\left[(\hat{u}_1\mathcal{U}_1 + \hat{u}_2\mathcal{U}_2)^2 + (\hat{v}_1\mathcal{U}_1 + \hat{v}_2\mathcal{U}_2)^2\right] \\
&= \frac{1}{2}\rho_0\left[\left(\hat{u}_1^2 + \hat{v}_1^2\right)\mathcal{U}_1^2 + \left(\hat{u}_2^2 + \hat{v}_2^2\right)\mathcal{U}_2^2 + 2(\hat{u}_1\hat{u}_2 + \hat{v}_1\hat{v}_2)\mathcal{U}_1\mathcal{U}_2\right],
\end{aligned}
\tag{9}
$$

where the last term on the rhs is the cross term, which disappears when depth integrating because of the orthogonality condition. If the mode 1 and 2 velocities are in phase at the surface the cross-term is positive, enhancing *KE*. At the same time, the mode 1 and 2 bottom velocities are out of phase near the bottom causing a negative cross term at depth, decreasing *KE*. In the resulting horizontal interference pattern, the amplified *KE* will always be largest near the surface because the $\mathcal{U}_n$ eigenfunctions have the largest values near the surface. The surface intensification of $\mathcal{U}_n$ is enhanced in the tropics due to the strong surface stratification (Wunsch, 2013). In the following we will show that the phase relation between the semidiurnal mode 1 and 2 waves (and thus the sign of the cross term) cause the banding patterns in surface energy and energy transfers.

The time-mean semidiurnal surface *KE* computed for the mode 1 velocities, the mode 2 velocities, and the sum of the mode 1 and mode 2 velocities (Equation 9) at the Bay of Bengal, Amazon Shelf, and Mascarene Ridge is shown in Figure 11. Surface *KE* is high for both mode 1 and mode 2 along the path of the internal tides in Figures 11a–11f, but the beams lack the banding patters. However, the constructive interference between mode 1 and 2 results in a banding pattern, which patches occur at the same locations as the undecomposed surface tidal *KE* in Figures 10g–10i (and the cross-scale energy transfer and supertidal flux divergence in Figures 10a–10f).

To further confirm the interference pattern between the mode 1 and 2 waves is surface intensified, we present the time-mean semidiurnal $KE(x, z)$ for modes 1 and 2 and nonlinear energy transfers along the Amazon internal tide beam in Figure 12. The patches of the surface intensified energy transfers near 50, 200, and 380 km in Figure 12d occur above the thermocline and coincide with enhanced surface tidal kinetic energy, computed from the superposed mode 1 and 2 velocities in Figure 12c. In contrast, the mode 1 and mode 2 *KE* in Figures 12a and 12b do not show these banding patterns.

The patches of nonlinear energy transfers in Figures 10a–10c and the flux divergence in Figures 10d–10f are large and positive adjacent to the ridges and shelf slopes, where gradients in topography and velocities are large. These gradients may contribute to strong nonlinear energy transfers. Although several mechanisms may explain these transfers (e.g., topographic lee waves), they are also attributed to the constructive interference between the semidiurnal mode 1 and 2 waves because the patches of elevated surface kinetic energy near topography in Figures 10g–10i, 11g–11i, and 12c occur in the same locations as the cross-scale energy transfers.

As the semidiurnal mode 1 and 2 waves propagate away from their generation sites, the faster mode 1 waves overtake the slower mode 2 waves. This causes alternating patterns of enhanced and reduced surface *KE* due to
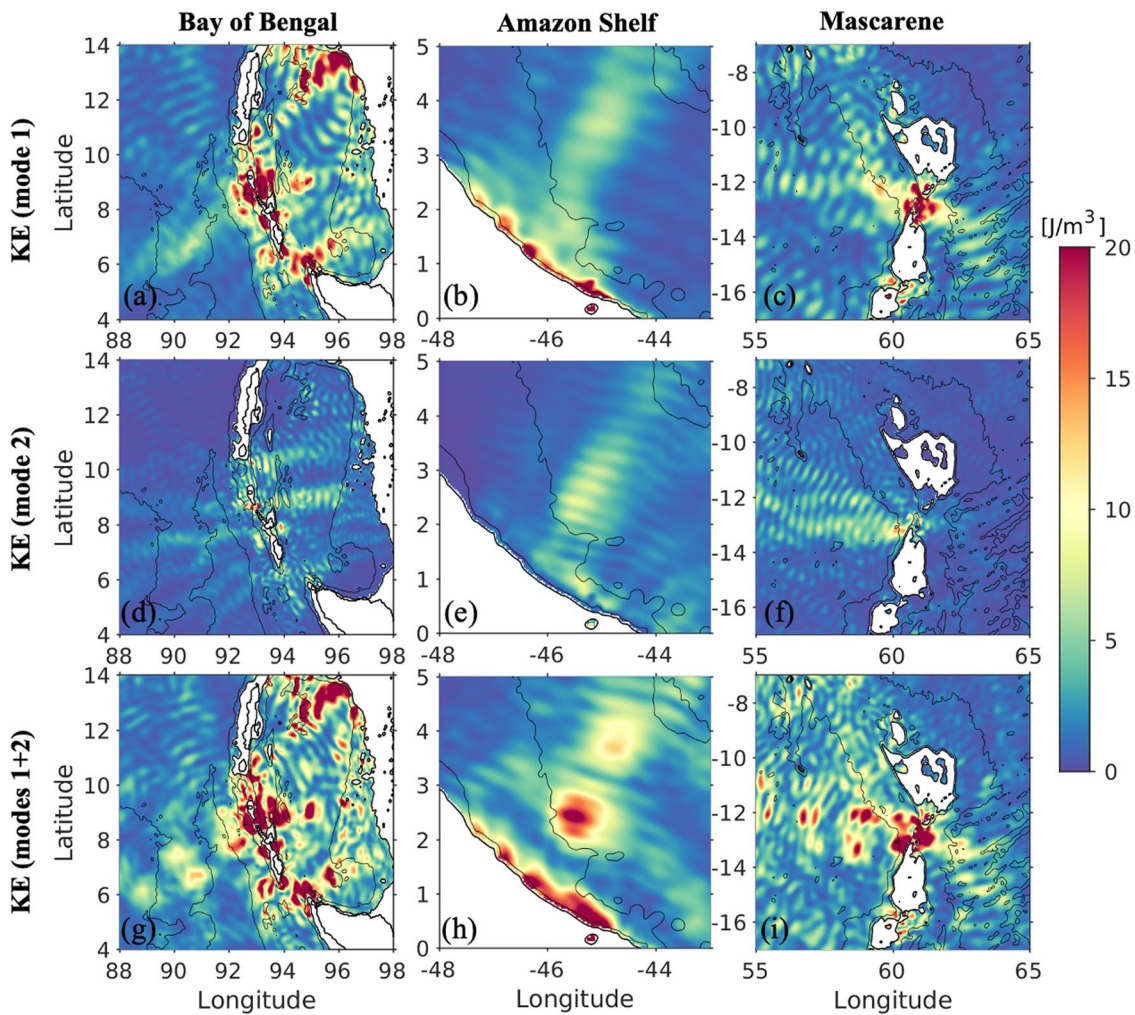
Figure 11. Time-mean surface kinetic energy (J/m³) for mode 1 at (a) the Bay of Bengal and Andaman Sea, (b) the Amazon Shelf, and (c) the Mascarene Ridge, (d–f) for mode 2 and (g–i) the sum of modes 1 and 2 for the same three areas. The contour lines mark the 0, 250, 1,000, and 3,500 m sea-floor depths.

positive and negative cross-term values in Equation 9. If we assume that the semidiurnal mode 1 and mode 2 waves are generated at the same time every tidal cycle with period T, the first patch occurs at the generation site and the second and each subsequent patch at a separation distance $\Delta S = \frac{c_1 c_2 T}{c_1 - c_2}$, where c_1 and c_2 are the M_2 mode 1 and 2 phase speeds. It follows from Table 1 that the predicted separation distance agrees well with the "observed" separation distance ΔS_o for the Bay of Bengal, the Amazon Shelf, and the Mascarene Ridge.

The banding patterns of surface intensified KE due to the constructive mode 1 and 2 superposition are distinct from the interference patterns associated with standing mode-1 waves. In the former, the separation distance is about 1.4–1.7 times the mode-1 wavelength (Table 1) and the pattern is only visible in surface KE (Figures 10g–10i), whereas in the latter, the separation distance between the KE maxima is 1/2 times the mode-1 wavelength (Buijsman et al., 2014; Martini et al., 2007; Rainville et al., 2010; Wang et al., 2018, 2021) and the maxima are visible in both surface and depth-integrated KE. For example, mode-1 standing wave patterns are clearly visible near 3°N and 47°W in Figures 10h and 10k and everywhere in Figures 11a–11c).

4.4. Temporal Modulation of Nonlinear Energy Transfers

Finally, we correlate the spatio-temporal variability of the 30-hr low-pass filtered nonlinear energy transfers to the 30-hr low-pass filtered semidiurnal modal surface KE, surface density, and supertidal SSH variance in Figure 13
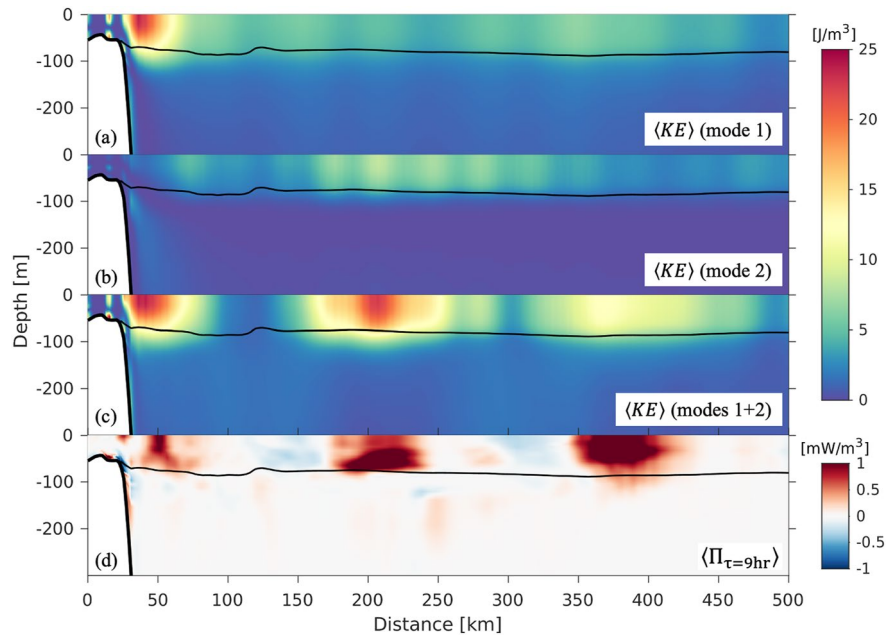
Figure 12. The time-mean semidiurnal kinetic energy (J/m^3) along a vertical transect aligned with the Amazon Shelf beam computed for (a) mode 1, (b) mode 2, and (c) the superposition of mode 1 and 2 velocities. (d) The time-mean coarse-grained kinetic energy transfer. The thick and thin black lines mark the sea-floor and pycnocline depth, respectively.

along the main internal tide beam at the Amazon Shelf. The regions of enhanced nonlinear forward energy transfer in Figure 13a near 50, 200, and 380 km coincide with enhanced surface KE for modes 1 + 2 in Figure 13b with a clear modulation by the spring-neap cycle.

Moreover, the regions of nonlinear energy transfers are also modulated by the slowly varying background flow and stratification. For example, the offshore migration of the density front associated with the Equatorial Currents at 300–350 km in Figure 13c coincides with an increase of the separation distance between the patches after 10 June. At the same time, the nonlinear energy transfers and the generation of NLIW in Figure 13d are reduced. Thus, the time varying background flow impacts the generation and propagation of tidal modes, which in turn affect the nonlinear energy transfers. The regular spaced banding patterns in SSSH are attributed to constructive interference between supertidal mode 1 and 2 waves.

If the nonlinear energy transfers are modulated by the slowly varying background flow and stratification on a monthly timescale in this study, we can also expect them to be modulated by seasonal changes. It has indeed been shown in several studies that the tidally generated NLIW can have a seasonal variability in amplitude and direction (e.g., Magalhaes et al., 2016; Tchilibou et al., 2022; Wijesekera et al., 2019; Zheng et al., 2007).

Table 1
The Comparison Between the Observed Separation Distance ΔS_o as Measured From the Maps and the Predicted Separation Distance $\Delta S = \frac{c_1 c_2 T}{c_1 - c_2}$

Area	ΔS_o (km)	ΔS (km)	c_1 (m/s)	c_2 (m/s)	L_1 (km)	L_2 (km)
Bay of Bengal	216	210	2.79	1.75	125	78
Amazon shelf	180	177	2.42	1.50	108	67
Mascarene ridge	190	185	2.95	1.72	132	77

Note. ΔS_o is the mean over several successive patch separation distances in deep water. The M_2 mode 1 and 2 phase speeds and wavelengths are area averaged in deep water. The M_2 tidal period $T = 12.417$ hr.

4.5. Synthesis

The regularly spaced banding patterns, for example, in semidiurnal surface KE, are not unique to our simulation. Similar patterns in semidiurnal SSSH variance at the same locations and with the same separation distances have been detected in satellite altimetry and regional model simulations of the Amazon Shelf region as shown in Figures 2c and 2d of Tchilibou et al. (2022). As in our simulations, the patches shown in Tchilibou et al. (2022) occur near 2.5° and 4°N along the main beam. We note that the banding patterns in semidiurnal SSSH variance in our HYCOM simulation occur at the same locations as the patterns in KE (result not shown).

These regularly spaced patches in surface intensified semidiurnal energy and SSSH variance are the locations of nonlinear energy transfers to
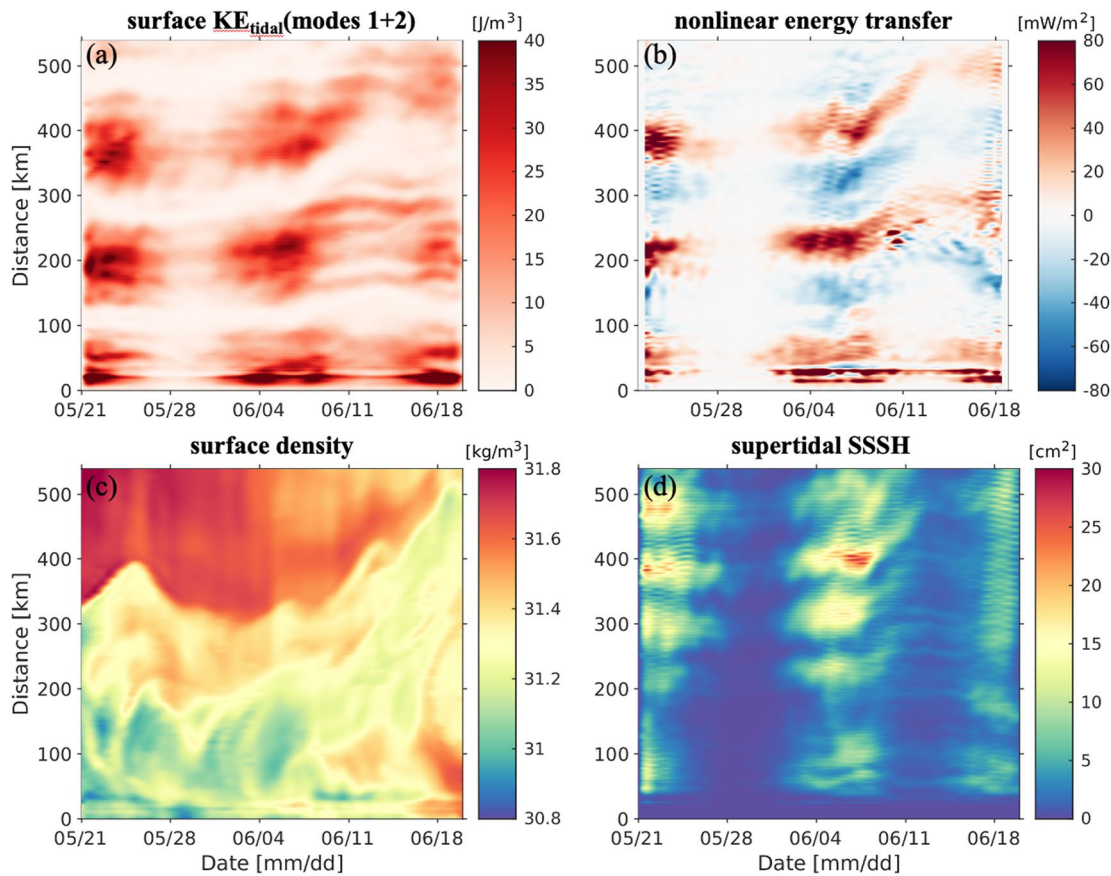
Figure 13. Hövmuller diagrams along the main internal tide beam at the Amazon Shelf of (a) nonlinear energy transfer to higher-harmonics, (b) semidiurnal surface kinetic energy computed from the sum of the mode 1 and 2 velocities, (c) surface density σ_2, and (d) the variance of supertidal steric sea surface height. All variables are 30-hr low-pass filtered to highlight subtidal modulations over the 30-day period.

higher harmonics. In our simulations these patches are due to constructive interference between semidiurnal mode 1 and 2 waves, which are generally the dominant modes radiating from tall ridges (Buijsman et al., 2020). Hence, maps of mode 1 and 2 interference could be used as a proxy to identify locations of nonlinear energy transfers, which are more cumbersome to compute. Similarly, maps of constructive interference between semidiurnal and diurnal modes and/or higher modes may also provide insight in the locations of these energy transfers.

The nonlinear energy transfers enhance the supertidal energy density in the equatorial region (Figure 2d), where f/N is small. These findings are in agreement with the theories of Gerkema and Zimmerman (1995) and Sutherland and Dhaliwal (2022) that predict the evolution of supertidal wave modes from mode-1 internal tides as they propagate equatorward where f is small and N is large. According to Sutherland and Dhaliwal (2022), the first step in this superharmonic energy cascade is a triad interaction of the primary frequency internal tide with itself, generating a mode-1 wave with a frequency that is moderately different from twice the internal tide frequency. The coincidence of the nonlinear energy transfers and the constructive interference between semidiurnal mode 1 and 2 waves at strong internal tide generation sites (Figures 10 and 11) suggest that these modes could be part of some type of wave-wave interaction, for example, resonant or near-resonant triads (Lamb, 2007; Varma & Mathur, 2017), if at all. However, an investigation in wave-wave interactions is beyond the scope of this paper and is reserved for a future study.

Internal tide dissipation due to wave-wave interactions is generally attributed to PSI (e.g., de Lavergne et al., 2019; Eden & Olbers, 2014; Pollmann et al., 2017). Ansong et al. (2018) diagnosed PSI in 4 and 8-km HYCOM simulations forced with either semidiurnal or diurnal tides. For the 4-km HYCOM simulation with semidiurnal tides, Ansong et al. (2018) estimated an energy transfer of 40 GW due to PSI out of the semidiurnal internal tide. The

energy transfer due to PSI in an 8-km simulation with diurnal tides was only 10 GW. The 40 GW is comparable to the 37 GW of net energy transfer from tidal to supertidal frequencies that we find in our study equatorward of $\pm25°$. This suggests that energy transfers out of low-mode internal tides due to nonlinear steepening cannot be ignored. We note that both subharmonic and superharmonic energy transfers increase significantly with finer grid spacings (Appendix A, Ansong et al., 2018; Nelson et al., 2020), pointing to the importance of small scale internal waves in resolving wave-wave interactions.

Finally, we note that the decay of the semidiurnal phase-locked (also referred to as stationary or coherent) internal tide in the equatorial Pacific as observed in satellite altimetry (Buijsman et al., 2017; Zaron, 2017; Zhao et al., 2016) may not be only attributed to the time variability of the equatorial currents and tropical instability waves, which scatters energy to the non-phase locked internal tide (Buijsman et al., 2017), but also to the energy transfer to higher harmonics (rectangles 4 and 5 in Figure 2d). For example, for the equatorward beam from the French Polynesian Islands (rectangle 5 in Figure 2d), the fraction of energy scattered to the non-phase locked tide (Figure 2b of Buijsman et al. (2017)) is comparable to the energy scattered to the supertidal band (20%–40%).

5. Conclusions

In this study we have for the first time diagnosed the depth-integrated and time-averaged supertidal energy budget in a realistically forced global HYCOM simulation. We have band-passed hourly 3D velocity and density fields over a 30-day period into diurnal (D1), semidiurnal (D2), and higher-harmonic (HH; supertidal) frequency bands and computed various energy terms. Depth-integrated kinetic energy and fluxes reveal horizontal internal tide beams at both tidal and supertidal frequencies. Tidal energy and fluxes are highest at internal tide generation sites and decay with distance from the source. However, supertidal energy and fluxes can peak a few hundred kilometers from the generation sites. The fluxes are dominated by the pressure flux, with the flux due to self advection being several orders of magnitude smaller for both the tidal and supertidal bands. At the strongest generation sites of super tidal energy, such as the Bay of Bengal, Amazon Shelf, and Mascarene Ridge, supertidal KE constitutes about 25%–50% of the KE summed over the tidal and supertidal bands. The zonally integrated supertidal kinetic energy is highest near the equator, where it accounts for about 10% of the total internal tide energy, and decreases toward higher latitudes. We estimate that on average, in the deep ocean (>250 m) and equatorward of $\pm25°$, supertidal KE accounts for about 5.4 PJ (~5%) of the total internal tide energy.

As opposed to the tidal flux divergence, the supertidal flux divergence does not correlate with the barotropic to baroclinic energy conversion, which is elevated at topography in the tidal band and near zero in the supertidal band. Instead, the time-mean and depth-integrated supertidal flux divergence correlates well with the nonlinear kinetic energy transfers from (sub)tidal to supertidal frequency bands as estimated with a novel coarse-graining approach. At the largest supertidal energy generation sites, both supertidal flux divergence and nonlinear energy transfers are organized in regularly spaced banding patterns with separation distances that are 1.4–1.7 times the semidiurnal mode-1 wavelength. These banding patterns are due to the constructive interference between semidiurnal mode 1 and 2 internal waves. The faster mode 1 wave overtakes the slower mode 2 wave, causing alternating patterns of reduced and elevated surface kinetic energy. Similar banding patterns have been observed in satellite altimetry and model simulations of the Amazon Shelf region by Tchilibou et al. (2022). These banding patterns are not present in KE after depth integration. We estimate that equatorward of $\pm25°$ about 37 GW, or about 7% of the tidal barotropic to baroclinic energy conversion, is transferred to higher-harmonics. This number is comparable to the net energy transfer out of the semidiurnal internal tide due to PSI (Ansong et al., 2018).

Areas in the open ocean with simulated supertidal energy fluxes >1 kW/m correlate well with observations of nonlinear solitary waves extracted from sunglint images (Jackson, 2007). We demonstrate for the Amazon Shelf, that as the tidal energy flux decays, the supertidal energy flux increases offshore. At the same time, the internal tide steepens into solitary waves, which surface expression agrees with SAR observations (Magalhaes et al., 2016). These simulated and observed solitary waves begin to appear near the second band of elevated nonlinear energy transfers at about 400 km from the shelf.

We acknowledge that our 4-km hydrostatic HYCOM simulation is only able to show the onset of the super-harmonic energy cascade that affects the low-mode internal tide. Higher resolution simulations are needed to properly simulate the spectral slopes at higher frequency and wavenumbers (Nelson et al., 2020). Furthermore, these simulations need to be nonhydrostatic to accurately simulate the nonhydrostatic solitary waves (Vitousek & Fringer, 2011), which is currently not yet feasible at global scales.

Appendix A: Effect of Grid Spacing

Solitary waves in the ocean have characteristic widths from a few hundred meters to several kilometers, and it is unclear how the grid spacing and hydrostatic approximation impact the steepening of the internal tide and energy transfer to higher-harmonics in global Hybrid Coordinate Ocean Model (HYCOM) simulations. To discuss this effect, we compare the internal tides in our simulation with a nonhydrostatic simulation that has a much higher resolution.

Internal solitary waves have been detected to the east of the Mascarene Plateau in the Indian Ocean using Synthetic Aperture Radar imagery and modeled using nonhydrostatic MITgcm simulations (da Silva et al., 2015). Both observations and simulations show large amplitude solitary waves appearing 50 km to the east of the sill after an internal tide beam steepens into NLIW. Leading solitons are observed to have widths of 800–4,200 m traveling at 1.9–2.8 m/s, with amplitudes of 70–200 m in the interior. Accurately simulating these NLIW in numerical models requires solving for nonhydrostatic pressure and horizontal grid spacings that are similar to the depth of the seasonal pycnocline to avoid numerical dispersion present in second order hydrostatic pressure gradient schemes (Vitousek & Fringer, 2011).

The 2-dimensional ($x - z$ plane) nonhydrostatic MITgcm simulation from da Silva et al. (2015) has a 100 m horizontal resolution and 200 layers in the vertical direction and was run over a 4-day period during a spring tide. The nonhydrostatic simulation displays a train of solitary waves with surface intensified velocities propagating along a transect in Figure A1a. In contrast, the HYCOM simulation along the same transect in Figure A1b does not show these steep nonlinear waves. The individual solitons in the MITgcm simulation have wavelengths of 1–2 km that are unresolved in our 4-km HYCOM simulation, although the large scale features of the internal tide agree well.

To provide a quantitative comparison of the relative importance of supertidal energy at this location we plot the percentage of supertidal energy along the transect in Figure A1c. In both simulations about 5% of the energy is found in the supertidal band at the reference (0 km), increasing to about 40% and 20% at 150 km in MITgcm and HYCOM, respectively. In agreement with other studies (e.g., Nelson et al., 2020), the higher resolution simulation allows for more efficient cross-scale energy transfers to smaller scales that are unresolved in the global HYCOM simulation, resulting in the underestimation of supertidal energy by about 50% at this location.
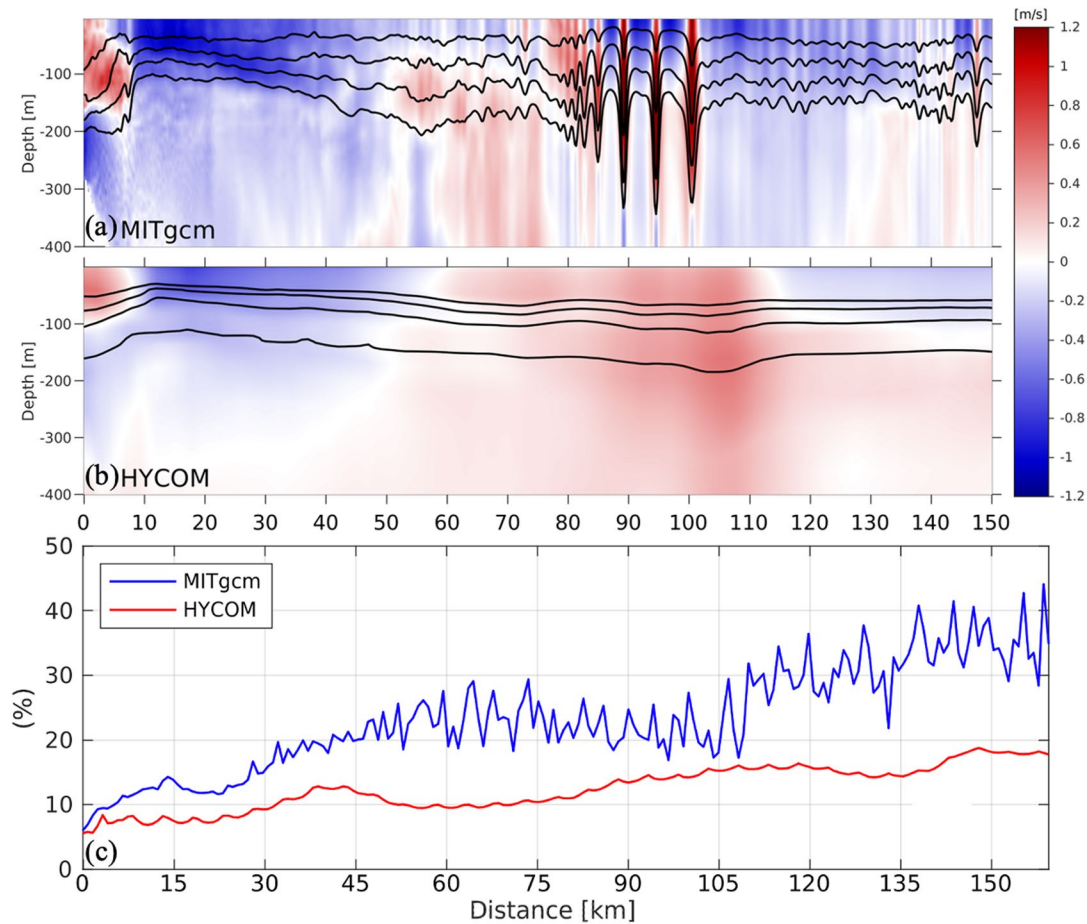
Figure A1. Vertical section at the east side of the Mascarene Ridge showing colormaps of instantaneous velocity from (a) the nonhydrostatic MITgcm simulation ($\Delta x = 100$ m) (da Silva et al., 2015) and (b) global Hybrid Coordinate Ocean Model ($\Delta x = 4$ km). The black curves in the top two panels denote the isopycnals at 1,031, 1,032, 1,033, and 1,034 kg/m^3. (c) Supertidal KE (2.67–12 cpd) as a fraction of the sum of the tidal and supertidal KE.

Appendix B: Nonlinear Parameters

To compare the nonlinear characteristics of the three generation sites Bay of Bengal, Amazon Shelf, and Mascarene Ridge, we compute two nonlinear internal wave parameters. A common measure of nonlinearity is the ratio of the wave amplitude to the depth of the time-averaged pycnocline $\alpha_a = A_0/h_1$ (e.g., Sutherland & Dhaliwal, 2022). Following Farmer et al. (2009), we assume a two-layer approximation and define the depth of the pycnocline h_1 as the depth of maximum buoyancy frequency averaged over 30 days. The amplitude A_0 of the nonlinear internal tide is defined as half the peak to trough vertical displacement at the pycnocline. The second measure of nonlinearity, useful when comparing to idealized simulations of weakly nonlinear waves (e.g., solutions to the KdV equation), is $\alpha_b = \frac{3}{2} c_0 \frac{h_1 - h_2}{h_1 h_2}$ (Farmer et al., 2009), where $h = h_1 + h_2$ is total water depth and c_0 is the linear long internal wave speed for a two-layer system. The nonlinear parameters α_a and α_b computed in the internal beams for the three sites are listed in Table B1. For reference, we also include in the table the time-mean and depth-integrated semidiurnal and supertidal energy flux magnitudes, and their ratios. They are computed at the same locations as the nonlinear parameters.

In agreement with the flux ratio, α_a and α_b have the largest values in the Bay of Bengal. In this region, the relatively shallow pycnocline results in stronger nonlinearities with similar wave amplitudes. The Amazon Shelf region has a deeper pycnocline and smaller wave amplitudes, while the Mascarene region has larger wave amplitudes but the much deeper pycnocline results in smaller nonlinearities. The study of Farmer et al. (2009) in the South China Sea ($h_1 = 500$ m, $h_2 = 2,500$ m, $c_0 = 3$ m/s, $A_0 = 50$ m) reports values of $\alpha_a = 0.1$ and $\alpha_b = 0.0072$, which are similar to the values that we find for the Mascarene Ridge and typical of weakly non-linear waves.

Table B1
Physical and Nondimensional Parameters for the Bay of Bengal (91.0°E, 7.7°N), Amazon Shelf (45.5°W, 2.45°N), and Mascarene Ridge (59.3°E, 12.0°S)

Region	h_1 (m)	h_2 (m)	c_0 (m/s)	A_0 (m)	α_a	α_b	F_{D2} (kW/m)	F_{HH} (kW/m) (%)
Bay of Bengal	245	3,175	2.72	51	0.15	0.015	11.5	3.8 (33.0)
Amazon shelf	306	3,441	2.46	36	0.12	0.011	14.5	3.5 (24.1)
Mascarene ridge	452	3,571	2.69	56	0.10	0.0056	12	2.5 (20.8)

Note. The ratio between the supertidal and semidiurnal energy flux magnitudes is listed in parentheses.

Data Availability Statement

The global time-mean and depth-integrated energy terms for HYCOM simulation EXPT 19.0 are published online as NetCDF files at https://doi.org/10.5281/zenodo.8284421. We have also included an example MATLAB script that can read these files. The SAR images used for extracting the crest lines in Figure 8 can be downloaded at https://dataspace.copernicus.eu/browser.

References

Alford, M. H., Peacock, T., Mackinnon, J. A., Nash, J. D., Buijsman, M. C., Centuroni, L. R., et al. (2015). The formation and fate of internal waves in the south China sea. *Nature*, *521*(7550), 65–69. https://doi.org/10.1038/nature14399

Alpers, W. (2018). Theory of radar imaging of internal waves. *Nature*, *314*(6008), 245–247. https://doi.org/10.1038/314245a0

Aluie, H., Hecht, M., & Vallis, G. K. (2018). Mapping the energy cascade in the north Atlantic Ocean: The coarse-graining approach. *Journal of Physical Oceanography*, *48*(2), 225–244. https://doi.org/10.1175/jpo-d-17-0100.1

Ansong, J. K., Arbic, B. K., Simmons, H. L., Alford, M. H., Buijsman, M. C., Timko, P. G., et al. (2018). Geographical distribution of diurnal and semidiurnal parametric subharmonic instability in a global ocean circulation model. *Journal of Physical Oceanography*, *48*(6), 1409–1431. https://doi.org/10.1175/JPO-D-17-0164.1

Arbic, B., Elipot, S., Brasch, J. M., Menemenlis, D., Ponte, A. L., Shriver, J. F., et al. (2022). Near-surface oceanic kinetic energy distributions from drifter observations and numerical models. *Journal of Geophysical Research: Oceans*, *127*(10), e2022JC018551. https://doi.org/10.1029/2022JC018551

Assene, F., Koch-Larrouy, A., Dadou, I., Tchilibou, M., Morvan, G., Chanut, J., et al. (2023). Internal tides off the amazon shelf part I: Importance for the structuring of ocean temperature during two contrasted seasons. *EGUsphere*, *2023*, 1–46. https://doi.org/10.5194/egusphere-2023-418

Baker, L. E., & Sutherland, B. R. (2020). The evolution of superharmonics excited by internal tides in non-uniform stratification. *Journal of Fluid Mechanics*, *891*, R1. https://doi.org/10.1017/jfm.2020.188

Barkan, R., Srinivasan, K., Yang, L., McWilliams, J. C., Gula, J., & Vic, C. (2021). Oceanic mesoscale eddy depletion catalyzed by internal waves. *Geophysical Research Letters*, *48*(18), e2021GL094376. https://doi.org/10.1029/2021GL094376

Bleck, R. (2002). An oceanic general circulation model framed in hybrid isopycnic-cartesian coordinates. *Ocean Modelling*, *4*(1), 55–88. https://doi.org/10.1016/S1463-5003(01)00012-9

Buijsman, M. C., Ansong, J. K., Arbic, B. K., Richman, J. G., Shriver, J. F., Timko, P. G., et al. (2016). Impact of parameterized internal wave drag on the semidiurnal energy balance in a global ocean circulation model. *Journal of Physical Oceanography*, *46*(5), 1399–1419. https://doi.org/10.1175/JPO-D-15-0074.1

Buijsman, M. C., Arbic, B. K., Richman, J. G., Shriver, J. F., Wallcraft, A. J., & Zamudio, L. (2017). Semidiurnal internal tide incoherence in the equatorial Pacific. *Journal of Geophysical Research: Oceans*, *122*(7), 5286–5305. https://doi.org/10.1002/2016JC012590

Buijsman, M. C., Kanarska, Y., & McWilliams, J. C. (2010). On the generation and evolution of nonlinear internal waves in the south China sea. *Journal of Geophysical Research*, *115*(C2), C02012. https://doi.org/10.1029/2009JC005275

Buijsman, M. C., Klymak, J. M., Legg, S., Alford, M. H., Farmer, D., MacKinnon, J. A., et al. (2014). Three-dimensional double-ridge internal tide resonance in Luzon strait. *Journal of Physical Oceanography*, *44*(3), 850–869. https://doi.org/10.1175/JPO-D-13-024.1

Buijsman, M. C., Stephenson, G. R., Ansong, J. K., Arbic, B. K., Green, J. A., Richman, J. G., et al. (2020). On the interplay between horizontal resolution and wave drag and their effect on tidal baroclinic mode waves in realistic global ocean simulations. *Ocean Modelling*, *152*, 101656. https://doi.org/10.1016/j.ocemod.2020.101656

Chen, M., Zhu, Z., Zhang, C., Zhu, X., Liu, Z., & Kaneko, A. (2021). Observation of internal tides in the qiongzhou strait by coastal acoustic tomography. *Journal of Ocean University of China*, *20*(5), 1037–1045. https://doi.org/10.1007/s11802-021-4590-x

da Silva, J. C., Buijsman, M. C., & Magalhaes, J. M. (2015). Internal waves on the upstream side of a large sill of the mascarene ridge: A comprehensive view of their generation mechanisms and evolution. *Deep-Sea Research Part I Oceanographic Research Papers*, *99*, 87–104. https://doi.org/10.1016/j.dsr.2015.01.002

de Lavergne, C., Falahat, S., Madec, G., Roquet, F., Nycander, J., & Vic, C. (2019). Toward global maps of internal tide energy sinks. *Ocean Modelling*, *137*, 52–75. https://doi.org/10.1016/j.ocemod.2019.03.010

Dunphy, M., Ponte, A. L., Klein, P., & Gentil, S. L. (2017). Low-mode internal tide propagation in a turbulent eddy field. *Journal of Physical Oceanography*, *47*(3), 649–665. https://doi.org/10.1175/JPO-D-16-0099.1

Eden, C., & Olbers, D. (2014). An energy compartment model for propagation, nonlinear interaction, and dissipation of internal gravity waves. *Journal of Physical Oceanography*, *44*(8), 2093–2106. https://doi.org/10.1175/JPO-D-13-0224.1

Eden, C., Pollmann, F., & Olbers, D. (2019). Numerical evaluation of energy transfers in internal gravity wave spectra of the ocean. *Journal of Physical Oceanography*, *49*(3), 737–749. https://doi.org/10.1175/JPO-D-18-0075.1

Egbert, G. D., & Ray, R. D. (2003). Semi-diurnal and diurnal tidal dissipation from TOPEX/Poseidon altimetry. *Geophysical Research Letters*, *30*(17), 1907. https://doi.org/10.1029/2003GL017676

Eyink, G. L., & Aluie, H. (2009). Localness of energy cascade in hydrodynamic turbulence. I. Smooth coarse graining. *Physics of Fluids*, *21*(11), 115107. https://doi.org/10.1063/1.3266883

Farmer, D., & Armi, L. (1999). The generation and trapping of solitary waves over topography. *Science*, *283*(5399), 188–190. https://doi.org/10.1126/science.283.5399.188

Farmer, D., Li, Q., & Park, J. (2009). Internal wave observations in the south China sea: The role of rotation and non-linearity. *Atmosphere-Ocean*, *47*(4), 267–280. https://doi.org/10.3137/OC313.2009

Gerkema, T. (2001). Internal and interfacial tides: Beam scattering and local generation of solitary waves. *Journal of Marine Research*, *59*(2), 227–255. https://doi.org/10.1357/002224001762882646

Gerkema, T., Staquet, C., & Bouruet-Aubertot, P. (2006). Non-linear effects in internal-tide beams, and mixing. *Ocean Modelling*, *12*(3–4), 302–318. https://doi.org/10.1029/2005GL025105

Gerkema, T., & Zimmerman, J. (1995). Generation of nonlinear internal tides and solitary waves. *Journal of Physical Oceanography*, *25*(6), 1081–1094. https://doi.org/10.1175/1520-0485(1995)025<1081:gonita>2.0.co;2

Grisouard, N., Staquet, C., & Gerkema, T. (2011). Generation of internal solitary waves in a pycnocline by an internal wave beam: A numerical study. *Journal of Fluid Mechanics*, *676*, 491–513. https://doi.org/10.1017/jfm.2011.61

Helfrich, K. R., & Grimshaw, R. H. J. (2008). Nonlinear disintegration of the internal tide. *Journal of Physical Oceanography*, *38*(3), 686–701. https://doi.org/10.1175/2007JPO3826.1

Hogan, T. F., Liu, M., Ridout, J. A., Peng, M. S., Whitcomb, T. R., Ruston, B. C., et al. (2014). The navy global environmental model. *Oceanography*, *27*(3), 116–125. https://doi.org/10.5670/oceanog.2014.73

Ivanov, V., Ivanov, L., & Lisichenok, A. (1990). Redistribution of energy of the internal tidal wave in the north equatorial countercurrent region. *Soviet Journal of Physical Oceanography*, *1*(5), 383–386. https://doi.org/10.1007/BF02196837

Jackson, C. R. (2007). Internal wave detection using the moderate resolution imaging spectroradiometer (MODIS). *Journal of Geophysical Research*, *112*(C11), C11012. https://doi.org/10.1029/2007JC004220

Jackson, C. R., da Silva, J., Jeans, G., Alpers, W., & Caruso, M. (2013). Nonlinear internal waves in synthetic aperture radar imagery. *Oceanography*, *26*(2), 68–79. https://doi.org/10.5670/oceanog.2013.32

Jackson, C. R., da Silva, J. C., & Jeans, G. (2012). The generation of nonlinear internal waves. *Oceanography*, *25*(2), 108–123. https://doi.org/10.5670/oceanog.2012.46

Jayne, S. R., & St. Laurent, L. C. (2001). Parameterizing tidal dissipation over rough topography. *Geophysical Research Letters*, *28*(5), 811–814. https://doi.org/10.1029/2000GL012044

Jensen, T. G., Magalhães, J., Wijesekera, H. W., Buijsman, M., Helber, R., & Richman, J. (2020). Numerical modelling of tidally generated internal wave radiation from the Andaman Sea into the Bay of Bengal. *Deep-Sea Research Part II Topical Studies in Oceanography*, *172*, 104710. https://doi.org/10.1016/j.dsr2.2019.104710

Jithin, A., & Francis, P. (2020). Role of internal tide mixing in keeping the deep Andaman Sea warmer than the Bay of Bengal. *Scientific Reports*, *10*(1), 11982. https://doi.org/10.1038/s41598-020-68708-6

Johnston, T. M. S., & Merrifield, M. A. (2003). Internal tide scattering at seamounts, ridges, and islands. *Journal of Geophysical Research*, *108*(C6), 1–17. https://doi.org/10.1029/2002JC001528

Kang, D., & Fringer, O. (2010). On the calculation of available potential energy in internal wave fields. *Journal of Physical Oceanography*, *40*(11), 2539–2545. https://doi.org/10.1175/2010JPO4497.1

Kang, D., & Fringer, O. (2012). Energetics of barotropic and baroclinic tides in the Monterey Bay area. *Journal of Physical Oceanography*, *42*(2), 272–290. https://doi.org/10.1175/JPO-D-11-039.1

Kelly, S. M. (2016). The vertical mode decomposition of surface and internal tides in the presence of a free surface and arbitrary topography. *Journal of Physical Oceanography*, *46*(12), 3777–3788. https://doi.org/10.1175/JPO-D-16-0131.1

Kelly, S. M., Lermusiaux, P. F., Duda, T. F., & Haley, P. J. (2016). A coupled-mode shallow-water model for tidal analysis: Internal tide reflection and refraction by the Gulf Stream. *Journal of Physical Oceanography*, *46*(12), 3661–3679. https://doi.org/10.1175/JPO-D-16-0018.1

Klymak, J. M., Simmons, H. L., Braznikov, D., Kelly, S., MacKinnon, J. A., Alford, M. H., et al. (2016). Reflection of linear internal tides from realistic topography: The Tasman continental slope. *Journal of Physical Oceanography*, *46*(11), 3321–3337. https://doi.org/10.1175/JPO-D-16-0061.1

Konyaev, K., Sabinin, K., & Serebryany, A. (1995). Large-amplitude internal waves at the mascarene ridge in the Indian Ocean. *Deep Sea Research Part I: Oceanographic Research Papers*, *42*(11–12), 2075–2091. https://doi.org/10.1016/0967-0637(95)00067-4

Lamb, K. G. (2004). Nonlinear interaction among internal wave beams generated by tidal flow over supercritical topography. *Geophysical Research Letters*, *31*(9), L09313. https://doi.org/10.1029/2003GL019393

Lamb, K. G. (2007). Tidally generated near-resonant internal wave triads at a shelf break. *Geophysical Research Letters*, *34*(18), L18607. https://doi.org/10.1029/2007GL030825

Legg, S. (2014). Scattering of low-mode internal waves at finite isolated topography. *Journal of Physical Oceanography*, *44*(1), 359–383. https://doi.org/10.1175/JPO-D-12-0241.1

Li, Z., & von Storch, J.-S. (2020). M_2 internal-tide generation in stormtide2. *Journal of Geophysical Research: Oceans*, *125*(8), e2019JC015453. https://doi.org/10.1029/2019JC015453

Luecke, C. A., Arbic, B. K., Richman, J. G., Shriver, J. F., Alford, M. H., Ansong, J. K., et al. (2020). Statistical comparisons of temperature variance and kinetic energy in global ocean models and observations: Results from mesoscale to internal wave frequencies. *Journal of Geophysical Research: Oceans*, *125*(5), e2019JC015306. https://doi.org/10.1029/2019JC015306

Mackinnon, J. A., Alford, M. H., Sun, O., Pinkel, R., Zhao, Z., & Klymak, J. (2013). Parametric subharmonic instability of the internal tide at 29°N. *Journal of Physical Oceanography*, *43*(1), 17–28. https://doi.org/10.1175/JPO-D-11-0108.1

Magalhaes, J. M., da Silva, J. C., & Buijsman, M. C. (2020). Long lived second mode internal solitary waves in the Andaman Sea. *Scientific Reports*, *10*(1), 10234. https://doi.org/10.1038/s41598-020-66335-9

Magalhaes, J. M., Silva, J. C. D., Buijsman, M. C., & Garcia, C. A. (2016). Effect of the north equatorial counter current on the generation and propagation of internal solitary waves off the amazon shelf (SAR observations). *Ocean Science*, *12*(1), 243–255. https://doi.org/10.5194/os-12-243-2016

Martini, K. I., Alford, M. H., Nash, J. D., Kunze, E., & Merrifield, M. A. (2007). Diagnosing a partly standing internal wave in Mamala Bay, Oahu. *Geophysical Research Letters*, *34*(17), L17604. https://doi.org/10.1029/2007GL029749

Mathur, M., Carter, G. S., & Peacock, T. (2014). Topographic scattering of the low-mode internal tide in the deep ocean. *Journal of Geophysical Research: Oceans*, *119*(4), 2165–2182. https://doi.org/10.1002/2013JC009152

Maxworthy, T. (1979). A note on the internal solitary waves produced by tidal flow over a three-dimensional ridge. *Journal of Geophysical Research*, *84*(C1), 338–346. https://doi.org/10.1029/JC084iC01p00338

Melet, A., Hallberg, R., Legg, S., & Polzin, K. (2013). Sensitivity of the ocean state to the vertical distribution of internal-tide-driven mixing. *Journal of Physical Oceanography*, *43*(3), 602–615. https://doi.org/10.1175/JPO-D-12-055.1

Mercier, M. J., Mathur, M., Gostiaux, L., Gerkema, T., Magalhães, J. M., Silva, J. C. D., & Dauxois, T. (2012). Soliton generation by internal tidal beams impinging on a pycnocline: Laboratory experiments. *Journal of Fluid Mechanics*, *704*, 37–60. https://doi.org/10.1017/jfm.2012.191

Metzger, E. J., Smedstad, O. M., Thoppil, P. G., Hurlburt, H. E., Cummings, J. A., Wallcraft, A. J., et al. (2014). US navy operational global ocean and arctic ice prediction systems. *Oceanography*, *27*(3), 32–43. https://doi.org/10.5670/oceanog.2014.66

Müller, M. (2013). On the space- and time-dependence of barotropic-to-baroclinic tidal energy conversion. *Ocean Modelling*, *72*, 242–252. https://doi.org/10.1016/j.ocemod.2013.09.007

Müller, M., Arbic, B. K., Richman, J. G., Shriver, J. F., Kunze, E. L., Scott, R. B., et al. (2015). Toward an internal gravity wave spectrum in global ocean models. *Geophysical Research Letters*, *42*(9), 3474–3481. https://doi.org/10.1002/2015GL063365

Muller, M., Cherniawsky, J., Foreman, M., & von Storch, J. (2012). Global M_2 internal tide and its seasonal variability from high resolution ocean circulation and tide modeling. *Geophysical Research Letters*, *39*(19), L19607. https://doi.org/10.1029/2012gl053320

Nash, J. D., Alford, M. H., & Kunze, E. (2005). Estimating internal wave energy fluxes in the ocean. *Journal of Atmospheric and Oceanic Technology*, *22*(10), 1551–1570. https://doi.org/10.1175/jtech1784.1

Nelson, A. D., Arbic, B. K., Menemenlis, D., Peltier, W. R., Alford, M. H., Grisouard, N., & Klymak, J. M. (2020). Improved internal wave spectral continuum in a regional ocean model. *Journal of Geophysical Research: Oceans*, *125*(5), e2019JC015974. https://doi.org/10.1029/2019JC015974

New, A. L., & Pingree, R. D. (1990). Large-amplitude internal soliton packets in the central Bay of Biscay. Deep Sea Research Part A. *Oceanographic Research Papers*, *37*(3), 513–524. https://doi.org/10.1016/0198-0149(90)90022-N

New, A. L., & Pingree, R. D. (1992). Local generation of internal soliton packets in the central Bay of Biscay. *Deep Sea Research Part A. Oceanographic Research Papers*, *39*(9), 1521–1534. https://doi.org/10.1016/0198-0149(92)90045-U

Ngodock, H. E., Souopgui, I., Wallcraft, A. J., Richman, J. G., Shriver, J. F., & Arbic, B. K. (2016). On improving the accuracy of the M_2 barotropic tides embedded in a high-resolution global ocean circulation model. *Ocean Modelling*, *97*, 16–26. https://doi.org/10.1016/j.ocemod.2015.10.011

Olbers, D. J. (1976). Nonlinear energy transfer and the energy balance of the internal wave field in the deep ocean. *Journal of Fluid Mechanics*, *74*(2), 375–399. https://doi.org/10.1017/S0022112076001857

Osborne, A. R., & Burch, T. L. (1980). Internal solitons in the Andaman Sea. *Science*, *208*(4443), 451–460. https://doi.org/10.1126/science.208.4443.451

Ostrovsky, L., & Stepanyants, Y. A. (1989). Do internal solitons exist in the ocean? *Review of Geophysics*, *27*(3), 293–310. https://doi.org/10.1029/rg027i003p00293

Pan, Y., Haley, P. J., & Lermusiaux, P. F. (2021). Interactions of internal tides with a heterogeneous and rotational ocean. *Journal of Fluid Mechanics*, *920*, A18. https://doi.org/10.1017/jfm.2021.423

Pollmann, F., Eden, C., & Olbers, D. (2017). Evaluating the global internal wave model idemix using fine structure methods. *Journal of Physical Oceanography*, *47*(9), 2267–2289. https://doi.org/10.1175/JPO-D-16-0204.1

Rainville, L., Johnston, T. M. S., Carter, G. S., Merrifield, M. A., Pinkel, R., Worcester, P. F., & Dushaw, B. D. (2010). Interference pattern and propagation of the M_2 internal tide south of the Hawaiian ridge. *Journal of Physical Oceanography*, *40*(2), 311–325. https://doi.org/10.1175/2009JPO4256.1

Raja, K. J., Buijsman, M. C., Shriver, J. F., Arbic, B. K., & Siyanbola, O. (2022). Near-inertial wave energetics modulated by background flows in a global model simulation. *Journal of Physical Oceanography*, *52*(5), 823–840. https://doi.org/10.1175/JPO-D-21-0130.1

Santos-Ferreira, A. M., da Silva, J. C. B., St-Denis, B., Bourgault, D., & Maas, L. R. M. (2023). Internal solitary waves within the cold tongue of the equatorial pacific generated by buoyant gravity currents. *Journal of Physical Oceanography*, *53*(10), 2419–2434. https://doi.org/10.1175/JPO-D-22-0165.1

Savage, A. C., Arbic, B. K., Richman, J. G., Shriver, J. F., Alford, M. H., Buijsman, M. C., et al. (2017). Frequency content of sea surface height variability from internal gravity waves to mesoscale eddies. *Journal of Geophysical Research: Oceans*, *122*(3), 2519–2538. https://doi.org/10.1002/2016JC012331

Savage, A. C., Waterhouse, A. F., & Kelly, S. M. (2020). Internal tide nonstationarity and wave–mesoscale interactions in the Tasman Sea. *Journal of Physical Oceanography*, *50*(10), 2931–2951. https://doi.org/10.1175/jpo-d-19-0283.1

Shriver, J. F., Arbic, B. K., Richman, J. G., Ray, R. D., Metzger, E. J., Wallcraft, A. J., & Timko, P. G. (2012). An evaluation of the barotropic and internal tides in a high-resolution global ocean circulation model. *Journal of Geophysical Research*, *117*(C10), C10024. https://doi.org/10.1029/2012JC008170

Simmons, H., Chang, M.-H., Chang, Y.-T., Chao, S.-Y., Fringer, O., Jackson, C. R., & Ko, D. S. (2011). Modeling and prediction of internal waves in the south China Sea. *Oceanography*, *24*(4), 88–99. https://doi.org/10.5670/oceanog.2011.97

Siyanbola, O. Q., Buijsman, M. C., Delpech, A., Renault, L., Barkan, R., Shriver, J. F., et al. (2023). Remote internal wave forcing of regional ocean simulations near the US west coast. *Ocean Modelling*, *181*, 102154. https://doi.org/10.1016/j.ocemod.2022.102154

Sutherland, B. R., & Dhaliwal, M. S. (2022). The nonlinear evolution of internal tides. Part 1: The superharmonic cascade. *Journal of Fluid Mechanics*, *948*, A21. https://doi.org/10.1017/jfm.2022.689

Tabaei, A., Akylas, T. R., & Lamb, K. G. (2005). Nonlinear effects in reflecting and colliding internal wave beams. *Journal of Fluid Mechanics*, *526*, 217–243. https://doi.org/10.1017/s0022112004002769

Tchilibou, M., Koch-Larrouy, A., Barbot, S., Lyard, F., Morel, Y., Jouanno, J., & Morrow, R. (2022). Internal tides off the amazon shelf during two contrasted seasons: Interactions with background circulation and SSH imprints. *Ocean Science Discussions*, *2022*, 1–38. https://doi.org/10.5194/os-2021-114

van Aken, H. M., van Haren, H., & Maas, L. R. M. (2007). The high-resolution vertical structure of internal tides and near-inertial waves measured with an ADCP over the continental slope in the Bay of Biscay. *Deep-Sea Research Part I Oceanographic Research Papers*, *54*(4), 533–556. https://doi.org/10.1016/j.dsr.2007.01.003

Varma, D., & Mathur, M. (2017). Internal wave resonant triads in finite-depth non-uniform stratifications. *Journal of Fluid Mechanics*, *824*, 286–311. https://doi.org/10.1017/jfm.2017.343

Venayagamoorthy, S. K., & Fringer, O. B. (2005). Nonhydrostatic and nonlinear contributions to the energy flux budget in nonlinear internal waves. *Geophysical Research Letters*, *32*(15), L15603. https://doi.org/10.1029/2005GL023432

Vic, C., Garabato, A. C. N., Green, J. A., Waterhouse, A. F., Zhao, Z., Melet, A., et al. (2019). Deep-ocean mixing driven by small-scale internal tides. *Nature Communications*, *10*(1), 2099. https://doi.org/10.1038/s41467-019-10149-5

Vitousek, S., & Fringer, O. B. (2011). Physical vs. numerical dispersion in nonhydrostatic ocean modeling. *Ocean Modelling*, *40*(1), 72–86. https://doi.org/10.1016/j.ocemod.2011.07.002

Wang, Y., Xu, Z., Hibiya, T., Yin, B., & Wang, F. (2021). Radiation path of diurnal internal tides in the northwestern pacific controlled by refraction and interference. *Journal of Geophysical Research: Oceans*, *126*(11), e2020JC016972. https://doi.org/10.1029/2020JC016972

Wang, Y., Xu, Z., Yin, B., Hou, Y., & Chang, H. (2018). Long-range radiation and interference pattern of multisource M_2 internal tides in the philippine sea. *Journal of Geophysical Research: Oceans*, *123*(8), 5091–5112. https://doi.org/10.1029/2018JC013910

Waterhouse, A. F., Mackinnon, J. A., Nash, J. D., Alford, M. H., Kunze, E., Simmons, H. L., et al. (2014). Global patterns of diapycnal mixing from measurements of the turbulent dissipation rate. *Journal of Physical Oceanography*, *44*(7), 1854–1872. https://doi.org/10.1175/JPO-D-13-0104.1

Wijesekera, H., Teague, W., Jarosz, E., Wang, D., Fernando, H., & Hallock, Z. (2019). Internal tidal currents and solitons in the southern Bay of Bengal. *Deep Sea Research Part II: Topical Studies in Oceanography*, *168*, 104587. https://doi.org/10.1016/j.dsr2.2019.05.010

Wunsch, C. (2013). Baroclinic motions and energetics as measured by altimeters. *Journal of Atmospheric and Oceanic Technology*, *30*(1), 140–150. https://doi.org/10.1175/JTECH-D-12-00035.1

Wunsch, C., & Ferrari, R. (2004). Vertical mixing, energy and the general circulation of the oceans. *Annual Review of Fluid Mechanics*, *36*(1), 281–314. https://doi.org/10.1146/annurev.fluid.36.050802.122121

You, J., Xu, Z., Li, Q., Robertson, R., Zhang, P., & Yin, B. (2021). Enhanced internal tidal mixing in the Philippine Sea mesoscale environment. *Nonlinear Processes in Geophysics*, *28*(2), 271–284. https://doi.org/10.5194/npg-28-271-2021

Yu, X., Ponte, A. L., Elipot, S., Menemenlis, D., Zaron, E. D., & Abernathey, R. (2019). Surface kinetic energy distributions in the global oceans from a high-resolution numerical model and surface drifter observations. *Geophysical Research Letters*, *46*(16), 9757–9766. https://doi.org/10.1029/2019GL083074

Zaron, E. D. (2017). Mapping the nonstationary internal tide with satellite altimetry. *Journal of Geophysical Research: Oceans*, *122*(1), 539–554. https://doi.org/10.1002/2016JC012487

Zhao, Z. (2014). Internal tide radiation from the Luzon strait. *Journal of Geophysical Research: Oceans*, *119*(8), 5434–5448. https://doi.org/10.1002/2014JC010014

Zhao, Z., Alford, M., Girton, J., Rainville, L., & Simmons, H. (2016). Global observations of open-ocean mode-1 M_2 internal tides. *Journal of Physical Oceanography*, *46*(6), 1657–1684. https://doi.org/10.1175/jpo-d-15-0105.1

Zheng, Q., Susanto, R. D., Ho, C.-R., Song, Y. T., & Xu, Q. (2007). Statistical and dynamical analyses of generation mechanisms of solitary internal waves in the northern south China Sea. *Journal of Geophysical Research*, *112*(C3), C03021. https://doi.org/10.1029/2006JC003551